Journal of Sound and Vibration (2000) **238**(5), 723–756
doi:10.1006/jsvi.1999.3109, available online at http://www.idealibrary.com on IDEAL®

EFFECT OF RADIAL INTERNAL CLEARANCE OF A BALL BEARING ON THE DYNAMICS OF A BALANCED HORIZONTAL ROTOR

M. Tiwari and K. Gupta

Mechanical Engineering Department, Indian Institute of Technology, Delhi, New Delhi 110016, *India.*
E-mail: tiwari.5@osu.edu

O. Prakash

Industrial Tribology Machine Dynamics and Maintenance Engineering Center, Indian Institute of Technology, Delhi, New Delhi 110016, *India*

(*Received* 30 *November* 1998, *and in final form* 30 *June* 1999)

The response of a balanced horizontal rigid motor rotor supported by a deep groove ball bearing is theoretically simulated. The effect of radial internal clearance of the ball bearing on the dynamic response of the rotor is studied. The system equations have been numerically integrated, the results of which have been validated with harmonic balance alternating frequency time domain method. Variation of radial internal clearance shifts the peak response as the speed is changed over a range. The results of a parametric study done by taking radial internal clearance have resulted in the observation of a third region of instability which has not been reported in literature. The appearance of regions of periodic, subharmonic and chaotic behavior is seen to be strongly dependent on the radial internal clearance. The system response is analyzed for stability and nature with the help of Floquets method for stability analysis and generation of higher order Poincare maps. The bearing stiffness is estimated experimentally and the effect of variation in radial internal clearance on the bearing stiffness is studied.

1. INTRODUCTION

The study of the dynamic response of a perfectly rigid and balanced, horizontal rotor supported by ball bearings is essentially a study of a non-linear system. The non-linearity is because of the radial internal clearance and the Hertzian contact between the races and the balls; there is also a parametric effect because of the varying compliance of the bearing.

The varying compliance effect was studied theoretically by Perret [1] considering a deep groove ball bearing with the elastic deformation between race and balls modelled by the Hertzian theory and no bending of races. Perret [1] studied the bearing at the instant when the balls are arranged symmetrically around the load line, i.e., with either a ball or a ball gap directly under the load. In the intermediate cage position, however, the balls are non-symmetrically arranged which means that when loaded vertically, the center of the inner ring will undergo a horizontal as well as vertical displacement. Meldau [2] studied theoretically the two-dimensional motion of shaft center. Both Perret [1] and Meldau [2] performed a quasi-static analysis since inertia and damping force were not taken into account.

0022-460X/00/500723 + 34 $35.00/0

Sunnersjo [3] studied the varying compliance vibrations theoretically and experimentally, taking inertia and damping forces into account. Fukata *et al.* [4] first took up the study of varying compliance vibrations and the non-linear dynamic response for the ball bearing supporting a balanced horizontal rotor with a constant vertical force. It is a more detailed analysis as compared to Sunnerjo's [3] work as regimes of super-harmonic, sub-harmonic and chaotic behavior are found out. Mevel and Guyader [5] have developed a theoretical model of a ball bearing supporting a balanced horizontal rigid rotor, with a constant vertical radial force. This is similar to the work done by Fukata *et al.* [4] but more results have been reported for parametric studies undertaken and routes to chaos traced out. Chaos in this model of bearing has been reported to come out of sub-harmonic route and quasi-periodic route.

Arc length continuation technique has been used for obtaining dynamic characteristics of ball bearings by Sankaravelu *et al.* [6]. This technique enables one to identify the possible parameter ranges for which the jump phenomena or the sudden change of the dynamic behavior of the system occurs. The ball bearing taken for study supports a constant vertical radial load of a balanced horizontal rotor. Sankaravelu *et al.* [6] have reported that the arc length continuation method takes less computation time as compared to direct integration, and the method obtains steady state response and stability analysis simultaneously. The eigenvalues of the Floquet matrix are obtained with the shooting technique which gives the bifurcation points. The system Sankaravelu *et al.* have taken for study is the same as that taken by Fukata *et al.* [4]. This work reports the appearance of chaotic response due to the intermittency. Once the stability sets in numerical integration is used to obtain the response. Tamura *et al.* [7] have theoretically estimated the stiffness of the ball bearing subjected to a constant radial load. Garguilo [8] has developed a new set of equations for providing initial estimates of stiffness of rolling element bearings.

Clearance in mechanical components introduces very strong non-linearity. The study of the effect of clearance non-linearity on the response of rotors has gained a lot of attention lately because of the development of high-speed rotors such as the space shuttle main engine turbo-pump rotor. Clearance non-linearity is different from most of the other non-linearities because it cannot be approximated by a mathematical series. Yamamoto [9] performed an analytical investigation of vibratory behavior of a vertical rotor supported on ball bearings with radial clearance. The conclusion of this work shows that the maximum amplitude at a critical speed and the value of critical speed decrease with increasing radial clearance. Childs [10] has studied the effect of non-symmetric clearance on rotor motion with the help of perturbation method under the assumption of small non-linearity. Saito [11] has reported the study of non-linear unbalance response of a horizontal Jeffcott rotor supported on ball bearings with radial clearance. The numerical harmonic balance technique has been used for calculating non-linear vibration of a rotor and an expression for the non-linear force is also given.

The study of excessive vibrations of the liquid oxygen pump in the space shuttle main engine pump by Childs and Moyer [12] and Beatty and Hine [13] during hot firing ground testing has shown that clearance non-linearity generates a frequency component incommensurate with rotation frequency. Day [14] carried out an analytical study of a rotor system supported on bearings with clearance. A special frequency named nonlinear natural frequency is defined and used to develop the solution of the non-linear Jeffcott rotor as singular asymptotic expansions. This non-linear frequency which is the ratio of cross stiffness and damping is incommensurate with respect to the rotational frequency. Kim and Noah [15] have studied a horizontal Jeffcott rotor supported on bearing with clearance. Harmonic balance/alternating frequency time domain (AFT) technique has been used for obtaining synchronous and sub-synchronous whirling motion of the rotor.

Ehrich [16] has analyzed theoretically the model of a Jeffcott rotor system operating eccentrically in a clearance and in local contact with stator possessing the characteristics of a bilinear oscillator. Sub-critical super-harmonic and super-critical subharmonic responses have been reported, which are shown to be mirror images of each other. Chaotic behavior and bifurcations can be observed. The response of the theoretical model compares well with the test data of an aero-engine gas turbine.

The dynamics of a shaft disk arrangement with clearance non-linearity at the supports has been dealt with by Flowers and Wu [17]. Numerical simulation and limit cycle analysis has been performed. Kim and Noah [18] have studied the theoretical model of Jeffcott rotor with bearing clearance, they have used a modified HBM/AFT method to obtain quasi-periodic response. The theoretical and experimental study of the non-linear effects introduced because of the ball bearing have not been reported. In this work, the effect of radial internal clearance has been studied, the appearance of subharmonics and Hopf bifurcation is seen theoretically whereas the shift in the peak response is also observed experimentally.

2. PROBLEM FORMULATION

The rotor-bearing system under study has the outer race of the ball bearing fixed to a rigid support and the inner race fixed rigidly to the shaft. A constant vertical radial force acts on the bearing. The excitation is because of the varying compliance vibrations of the bearing which arise because of the geometric and elastic characteristics of the bearing assembly varying according to the cage position.

The ball bearing model considered here has equispaced balls rolling on the surfaces of the inner and outer races. For developing the theoretical model it is assumed that the outer race is fixed rigidly to the support and the inner race is fixed rigidly to the shaft and there is no bending of races. There is perfect rolling of balls on the races so that the two points of the ball (A and B) touching the outer and inner races have different linear velocities (Figure 1). The center of the ball has a resultant translational velocity. Therefore,

$$\omega_{cage} = \omega_{ROTOR}\left(\frac{R_i}{R_i + R_O}\right). \tag{1}$$

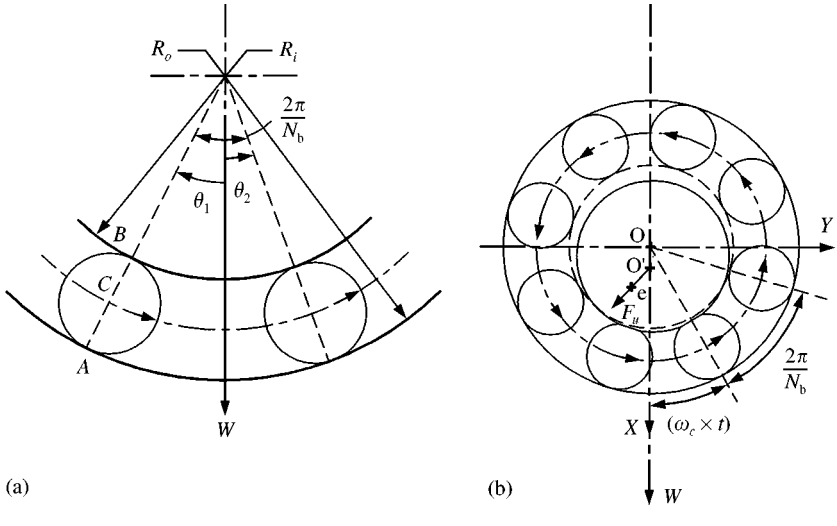

Figure 1. Ball bearing.

The varying compliance frequency is given by

$$\omega_{vc} = \omega_{cage} \times N_b, \tag{2}$$

where N_b is the number of balls. From equation (1), we can write

$$\omega_{vc} = \omega_{ROTOR} \times BN, \tag{3}$$

where

$$BN = \frac{R_i}{R_i + R_O} \times N_b. \tag{4}$$

The number BN depends on the dimensions of the bearing, for SKF6002, $BN = 3{\cdot}6$.

The damping of a ball bearing is very small; this is because of friction and small amount of lubrication. The estimation of damping of a ball bearing is very difficult because of the dominant extraneous damping which swamps the damping of the bearing. Krämer [19] has provided an estimation of the bearing damping.

$$f_{eq} = \frac{\omega_{eq}}{2\pi} = (0{\cdot}4\text{–}4)\,10^5 \text{ s}^{-1}$$

$$d = (0{\cdot}25\text{–}2{\cdot}5)\,10^{-5}\,K \text{ (N s/}\mu\text{m)}, \tag{5}$$

where K is the linearized stiffness of the ball bearing.

The linearized stiffness can be estimated from the method given by Tamura [7] or Gargiulo [8]. The bearing is assumed to be free of local and distributed defects. The balls are arranged equispaced around the bearing and move around the race with equal velocity, which is physically possible because of the cage. The radial internal clearance is the clearance between an imaginary circle, which circumscribes the balls and the outer race. This clearance is also called the play in the bearing. For a horizontal rotor as the shaft settles down due to the radial constant force W, the radial internal clearance closes in the angular contact zone [20]. The ball–race contact deformation of the ball generates a restoring force with non-linear characteristics because of the Hertzian contact.

$$F_{\theta_i} = C_b(r_{\theta_i})^n, \quad n = 3/2. \tag{6}$$

The values of C_b and n are arrived at by performing the elastic analysis of the Hertzian contact between the inner and outer race and the ball [20]. For SKF6002 $C_b = 7{\cdot}055 \times 10^9$ N/m$^{3/2}$. Taking the x and y displacements of the center of the inner race

$$F_{\theta_i} = C_b(x \cos\theta_i + y \sin\theta_i - \gamma_0)_+^{1{\cdot}5}. \tag{7}$$

If the expression inside the brackets is greater than zero, then the ball at angular location θ_i is loaded giving rise to a restoring force F_{θ_i}. If the expression in the brackets is negative or zero, then the ball is not in the load zone, and the restoring force F_{θ_i} is set to zero. The " + " sign as a subscript in equation (11) signifies the above. The total restoring force is the sum of the restoring force from each of the rolling elements. Thus, the total restoring force

TABLE 1

Bearing damping

	SKF 6002 ($W = 6$ N)	Fukata ($W = 58{\cdot}8$ N)
K (N/m)	$13{\cdot}5 \times 1{\cdot}0^6$	42×10^6
d (N s/m)	33·75–337·5	105–1050

components in the X and Y directions are

$$F_x = C_b \sum_{i=1}^{N_b} (x \cos\theta_i + y \sin\theta_i - \gamma_0)_+^{1{\cdot}5} \cos\theta_i,$$
$$F_y = C_b \sum_{i=1}^{N_b} (x \cos\theta_i + y \sin\theta_i - \gamma_0)_+^{1{\cdot}5} \sin\theta_i, \tag{8}$$

As the shaft rotates, the angle θ_i changes with time (Figure 1) and is given by

$$\theta_i = \frac{2\pi}{N_b}(i-1) + \omega_{cage} \times t, \quad i = 1, \ldots, N_b. \tag{9}$$

Here the reference is the vertical axis which is the direction of the constant vertical force. We see that θ_i is a function of time and this imparts the parametric effect to the system.

The damping in this system is represented by an equivalent viscous damping C. The value of the damping depends on the linearized bearing stiffness (5). The value of the damping has been estimated (Table 1). The system governing equations accounting for inertia, restoring and damping force and constant vertical force acting on the inner race are,

$$m\ddot{x} + C\dot{x} + C_b \sum_{i=1}^{N_b} (x \cos\theta_i + y \sin\theta_i - \gamma_0)_+^{1{\cdot}5} \cos\theta_i = W + F_u \cos(\omega t),$$
$$m\ddot{y} + C\dot{y} + C_b \sum_{i=1}^{N_b} (x \cos\theta_i + y \sin\theta_i - \gamma_0)_+^{1{\cdot}5} \sin\theta_i = F_u \sin(\omega t). \tag{10}$$

Here m is the mass of the rotor supported by bearing and mass of inner race. The imbalance force F_u for this case is zero. System (14) consists of two coupled non-linear ordinary second order differential equations having a parametric effect in them. The stiffness because of its step change behavior, the parametric effect with 1·5 non-linearity and the summation term is non-analytic in nature.

3. METHODS OF SOLUTION

The two coupled non-linear sound order differential equations are solved by numerical integration which is a time domain approach as well as by the harmonic balance/alternating frequency time (AFT) domain technique. The non-analytic nature of the stiffness term renders the system equations difficult for analytical solution.

3.1. NUMERICAL INTEGRATION

For performing numerical integration, the system equations are transformed into first order form by introducing two variables z_1 and z_2.

$$z_1 = \dot{x}, \qquad z_2 = \dot{y},$$

$$\dot{z}_1 = \frac{W}{m} - \frac{C}{m} z_1 - \frac{C_b}{m} \sum_{i=1}^{N_b} (x \cos\theta_i + y \sin\theta_i - \gamma_0)_+^{1\cdot5} \cos\theta_i,$$

$$\dot{z}_2 = -\frac{C}{m} z_2 - \frac{C_b}{m} \sum_{i=1}^{N_b} (x \cos\theta_i + y \sin\theta_i - \gamma_0)_+^{1\cdot5} \sin\theta_i. \tag{11}$$

Since the right-hand side depends on time the system is non-autonomous.

These equations were found to be numerically stiff. Comparin and Singh [21] have pointed out that systems with clearance non-linearity are frequently afflicted by numerical stiffness. The numerical integration method used in the present analysis is based on the Cash–Karp Runge–Kutta method (RKCK). It was seen that the RKCK method [22] took 3 times more CPU time as compared to the NAG Subroutine based on the backward differentiation method which is of implicit type. The RKCK method is a fifth order explicit-type Runge–Kutta method.

3.1.1. *Choice of step size and initial condition*

The RKCK method has a provision for estimating local truncation error by comparing with embedded fourth order Runge–Kutta method. For various speeds and a damping value of 200 Ns/m and $W = 6$ N, the system was numerically integrated on a Silicon Graphics work station for a number of time step sizes. The local truncation error and CPU time are plotted against the step size in Figure 2. We can see that region AA′ gives the best results. Accordingly, a step size of 1×10^{-4} s is chosen in all subsequent calculations.

3.2. MODIFIED HARMONIC BALANCE METHOD

The harmonic balance method (HBM) has been applied for solving the system equations (10). The presence of non-analytic stiffness terms suggests a need for modification of the HBM, for which the alternating frequency time (AFT) domain technique is used [23]. Rotor-bearing systems with clearance non-linearity at the support have been found to have

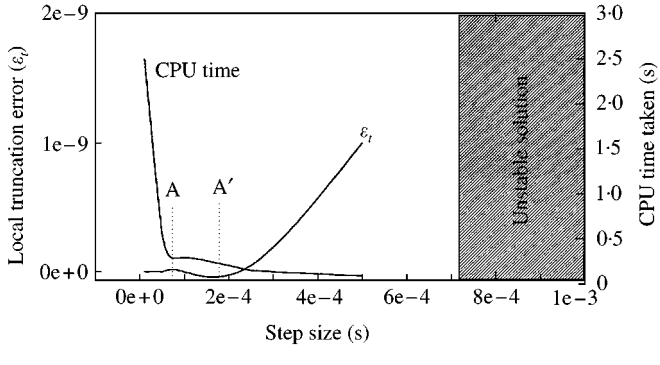

Figure 2. Effect of step size.

amplitude-modulated response [12, 14, 18]. Also, for the rotor bearing system considered it is seen from numerical integration solutions that under certain conditions response has amplitude modulation. Taking the interaction between the two frequencies only, i.e., carrier and modulated frequency, a double-harmonic generalized series is needed to express x, y and the non-linear force terms.

$$X(t) = \sum_{i=0}^{N} \sum_{j=-N}^{N} [a_{X_{ij}} \cos(v_{ij}t) - b_{X_{ij}} \sin(v_{ij}t)],$$

$$Y(t) = \sum_{i=0}^{N} \sum_{j=-N}^{N} [a_{Y_{ij}} \cos(v_{ij}t) - b_{Y_{ij}}(v_{ij}t)]. \tag{12}$$

Here, $v_{ij} = \mathrm{i}\omega_1 + \mathrm{j}\omega_2$, $i, j = 1, 2, \ldots$. Also, ω_1 and ω_2 are the carrier and the modulating frequencies respectively. The non-analytic non-linear spring force terms are also represented by similar double-harmonic series.

$$F_{nx}(t) = \sum_{i=0}^{N} \sum_{j=-N}^{N} (c_{X_{ij}} \cos(v_{ij}t) - d_{X_{ij}} \sin(v_{ij}t)],$$

$$F_{ny}(t) = \sum_{i=0}^{N} \sum_{j=-N}^{N} (c_{Y_{ij}} \cos(v_{ij}t) - d_{Y_{ij}} \sin(v_{ij}t)]. \tag{13}$$

The coefficients of sin and cos in the series representing non-linear force terms are functions of displacements X and Y. The harmonic series representing the displacements and non-linear force terms is not an ordinary Fourier series because the frequency spectra, $v_{ij} = i\omega_1 + j\omega_2$ (where $i = 0, \ldots, N; j = -N, \ldots, 0, \ldots, +N$) are not harmonically related. The harmonic series are almost periodic functions [24]. The series in equation (12) can be differentiated with respect to time to give corresponding series for velocity and acceleration.

Substituting the series for displacement, velocity and acceleration into system (10) and equating coefficients of cos, sin and constant terms on both sides of the equations, we get nonlinear algebraic equations with coefficients of generalized harmonic series as the variables. Comparisons of constant terms on both sides of the two equations give

$$g(1) = C_b \times c_{X_{00}} - W,$$

$$g(2) = C_b \times c_{Y_{00}}, \tag{14}$$

by comparing coefficients of sin and cos on both sides, we get the following relations:

$$\text{for } l \geqslant 3,\ i = 1,\ N_i \text{ and } j = -N_j, \ldots, 0, \ldots, N_j \qquad (i \neq 0 \text{ and } j \neq 0),$$

$$\begin{aligned}
g(1) &= -m \times v_{ij}^2 \times a_{X_{ij}} - C_d \times v_{ij} \times b_{X_{ij}} + C_b \times c_{X_{ij}},\\
g(l+1) &= m \times v_{ij}^2 \times b_{X_{ij}} - C_d \times v_{ij} \times a_{X_{ij}} - C_b \times d_{X_{ij}},\\
g(l+2) &= -m \times v_{ij}^2 \times a_{Y_{ij}} - C_d \times v_{ij} \times b_{Y_{ij}} + C_b \times c_{Y_{ij}},\\
g(l+3) &= m \times v_{ij}^2 \times b_{Y_{ij}} - C_d \times v_{ij} \times a_{Y_{ij}} - C_b \times d_{Y_{ij}}.
\end{aligned} \tag{15}$$

For solving this set of non-linear algebraic equations the coefficients of the series have to be determined. Since the series are not Fourier series the discrete Fourier transform (DFT)

algorithms cannot be used for estimating the coefficients. The coefficients are determined by minimizing the mean square error between the exact steady state solution and the solution from the series [24]. The generalized series can now be expressed in the following form:

$$X(t) = [\Gamma]\{L_x\}, \qquad Y(t) = [\Gamma]\{L_y\}, \tag{16}$$

where $\{L_x\}$ and $\{L_y\}$ are matrices with components as coefficients of the series for X and Y respectively. The coefficients of the generalized series representing the displacements X and Y are estimated by

$$\{\hat{L}_x\} = (\Gamma^{\mathrm{T}}\,\Gamma)^{-1}\Gamma^{\mathrm{T}}X_{ss}(t), \qquad \{L_x\} = \{\hat{L}_X\} + \varepsilon(M). \tag{17}$$

Similarly for $\{L_y\}$. Also, $X_{ss}(t)$ and $Y_{ss}(t)$ are the steady state solutions and $\varepsilon(M)$ is the error such that $\varepsilon(M) \to 0$ as $M \to \infty$. This simply implies that as the number of time samples (M) is increased, the approximate generalized series $X(t)$ comes closer to the exact steady solution $X_{ss}(t)$ (similarly for $Y(t)$).

The non-linear force terms are functions of known displacements X and Y.

$$F_X(M\Delta t) = C_b \sum_{i=1}^{M_b} (x(M\Delta t)\cos\theta_i + y(M\Delta t)\sin\theta_i - \gamma_0)_+^{1.5}\cos\theta_i,$$

$$F_Y(M\Delta t) = C_b \sum_{i=1}^{N_b} (x(M\Delta t)\cos\theta_i + y(M\Delta t)\sin\theta_i - \gamma_0)_+^{1.5}\sin\theta_i. \tag{18}$$

The coefficients of the generalized Fourier series representing the non-linear force terms are components of $\{M_x\}$ and $\{M_y\}$. From the method of minimization of least squares, we can write

$$\{M_X\} = (\Gamma^{\mathrm{T}}\,\Gamma)^{-1}\Gamma^{\mathrm{T}}F_{nx}(M\Delta t), \quad \{M_Y\} = (\Gamma^{\mathrm{T}}\,\Gamma)^{-1}\Gamma^{\mathrm{T}}F_{nY}(M\Delta t). \tag{19}$$

These coefficients are used with $\{L_X\}$ and $\{L_Y\}$ to estimate the value of $g(i)$ $(i = 1, \ldots,)$. These non-linear algebraic equations are solved by Broyden's method [22].

The steady state solution which is needed for this method is obtained by numerical integration of the system equations with initial conditions as the fixed points of the system which ensures a steady state solution. This HBM/AFT technique has been used to validate the solution obtained from numerical integration and also to find such solutions which are not possible with numerical integration.

For the case when the modulating frequency $\omega_2 = 0$ or ω_2 is a subharmonic of ω_1, the generalized Fourier series turns into a proper Fourier series with periodic frequency spectra υ_{ij} (period T) [25] if

$$\Delta t = \frac{T}{M}. \tag{20}$$

Here T is the least common period of the system and M is the number of samples taken for finding out steady state solution. In the present analysis, convergence occurred for $M = 5$(N). Broyden's method converged and gave a solution when the initial steady state solution was taken for a neighboring parameter combination. For a combination not close, there was no convergence. For finding out multiple solutions (in regions of multivalued solutions), the steady state solution X_{ss} and Y_{ss} was taken for the solution possible with numerical integration, and the frequencies ω_1 and ω_2 were set for the desired solution. This method is used only for validating the numerical integration solutions since a solution has to be known *a priori*. Also, this procedure is inefficient in terms of computation time when

many frequency components are present. Moreover, it is not possible to apply this method in chaotic region.

4. BEARING STIFFNESS

The linearized bearing stiffness is estimated by the Tamuras [7] method where W is the constant radial force, N_b is the number of balls, and C_b is the spring constant obtained from Hertzian analysis. X is the axis along the direction of the vertical constant force W and Y is the axis perpendicular to the direction of X

$$\begin{bmatrix} \partial F_X/\partial x \\ \partial F_Y/\partial y \end{bmatrix} = W^{1/3}(N_b C_b)^{2/3} \begin{bmatrix} 1/\Phi_1(\Gamma) \\ \Phi_2(\Gamma) \end{bmatrix}, \quad \frac{\partial F_X}{\partial y} = \frac{\partial F_y}{\partial x} = 0, \tag{21}$$

Φ_1 and Φ_2 are functions of dimensionless number Θ [7]

$$\Theta = \gamma_0/(W/NC_b)^{2/3} \tag{22}$$

or

$$\Theta \equiv \frac{N^{(3/2)}}{2}\left(\cot^2\frac{\pi}{N} - 1\right), \tag{23}$$

whichever expression gives minimum value of Θ.

5. METHODS OF ANALYSIS

To analyze the results obtained from numerical integration various techniques are used for studying the stability and nature of solutions. Higher order Poincare maps are generated for studying the nature of solutions if it is harmonic, subharmonic, or chaotic. For finding out the fixed point of the system at a particular speed the non-autonomous shooting method is used. The stability of the solution is found by the Floquets method [28] which also gives the monodromy matrix from which the nature of bifurcation is known.

6. RESULTS AND DISCUSSION

The algorithms developed for the solution of the equations and the analysis have been applied for the reported work by Fukata [4] for JIS6306 and the results match very well [26]. In the present study for an SKF6002 ball bearing the radial internal clearance is taken as the main parameter of study, which has not been reported by Fukata [4], Mevel and Guyader [5] and Sankaravelu [6].

6.1. STATIC BEARING STIFFNESS

In the present work, an SKF6002 bearing supports a rigid horizontal rotor with no imbalance force. The reported works by Fukata *et al.* [4], Mevel and Guyader [5] and Sankaravelu [6] have taken the case of a deep groove ball bearing JIS6306.

The static stiffness has been estimated for two levels of vertical force 6 and 24 N. From Figure 3 it can be seen that for SKF6002 the stiffness (natural frequency for $m = 0{\cdot}6$ kg)

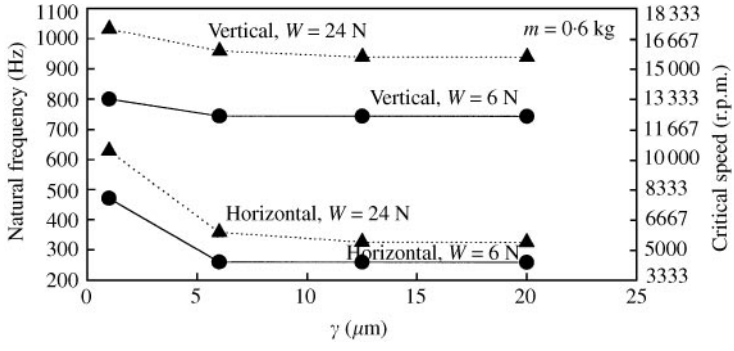

Figure 3. Vertical and horizontal critical frequency.

remains practically constant till a radial internal clearance of 6 μm ($W = 6$ N) for both values of vertical force. As the clearance is reduced further, stiffness increases in all cases. Natural frequency in the vertical direction is more than that in the horizontal direction. The natural frequency is found to increase with increasing load for both the vertical and horizontal directions. The critical speed for the balanced case is given by the speed at which the varying compliance (exciting) frequency equals the natural frequency.

6.2. RESULTS OF THEORETICAL SIMULATION

The work reported in references [4–6] have focused more on a parametric effect involving speed change and damping of ball bearings. In this work, besides speed as a parameter of study, the effect of radial internal clearance is also studied. The radial internal clearance is an important parameter of study because even if it is inevitable, it can be controlled to a good extent.

For theoretical simulation the values of radial internal clearance taken are 20, 12, 6 and 1 μm. For each of these clearance values, two values of damping 340 and 200 N s/m are taken. The higher value of 340 N s/m is representative of the extreme value and the lower value of 200 N s/m represents a medium level of damping in SKF 6002 with $m = 0{\cdot}6$ kg and $W = 6$ N.

Speed response plots are obtained for the combination of the above parameters under study. These plots are generated by numerical integration to reach steady state when peak-to-peak values of x and y displacements are obtained. For reaching steady state for the first speed the initial conditions are taken as the fixed point solution. For successive speeds, the initial conditions are taken as the steady state solution obtained for the preceding speed. For a non-linear system the response plots have regions of multivalued solution [27] which are generally the high-amplitude regions. Generating the response curve so that the ith steady state speed solution is near the $(i-1)$th speed solution ensures that the same response curve is plotted throughout, otherwise there is a danger of the solution jumping from one response curve to another. Multi-solutions are obtained easily with the help of the HBM/AFT technique when the solution does not have many frequency components and the frequency content of the multivalued solutions is known *a priori*.

6.2.1. $\gamma_0 = 20\ \mu m,\ C = 200\ N\,s/m,\ W = 6\ N$

The overall response plot is shown in Figure 4. The peak-to-peak (pp) vertical response is less than the peak-to-peak horizontal response in regions of high amplitude. The overall

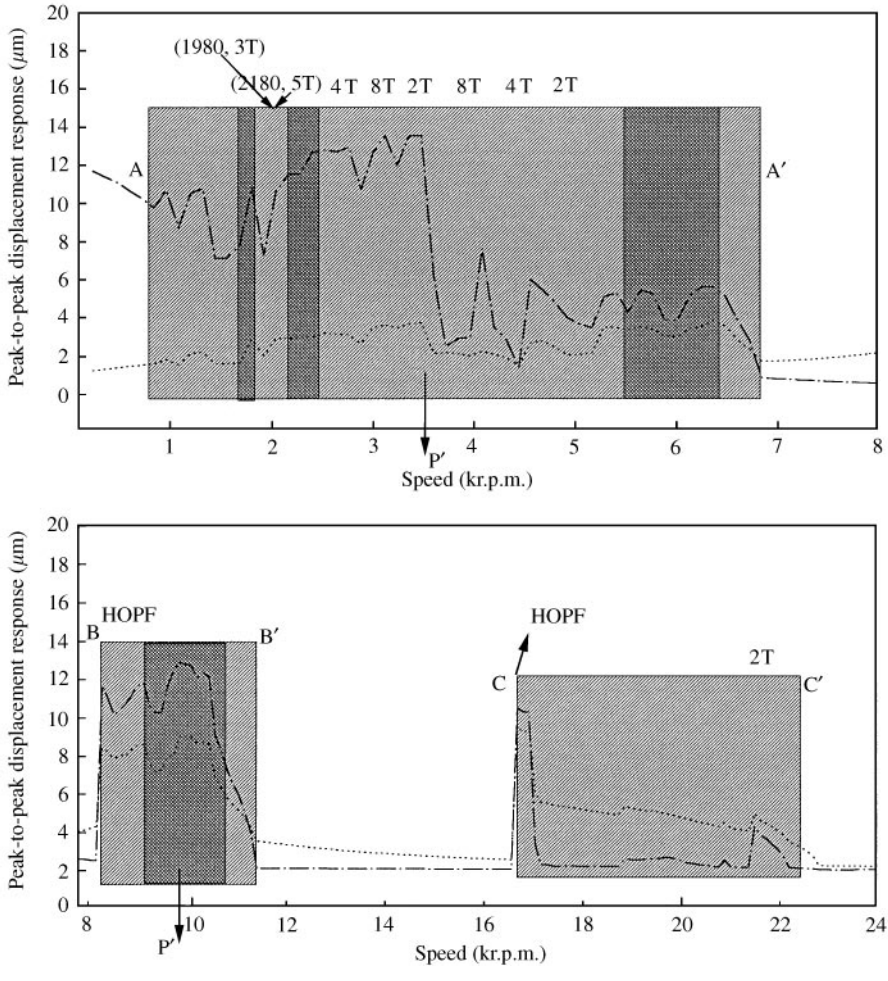

Figure 4. Response plot, $\gamma_0 = 20$ μm, C = 200 N s/m, $W = 6$ N; ▩, period 1 unstable; ▨, chaotic regime; · · · · · ·, vertical; – · –, horizontal.

response plot has a very rough appearance. Three regions can be identified which have high pp response. These regions are shown in Figure 4, bounded by lines A–A′, B–B′ and C–C′. Figures 5(a, b) give the response plots of peak-to-peak amplitude of frequency components corresponding to varying compliance (VC) frequency 1/2 VC, 1VC, 2VC, 3VC, 4VC and 5VC. The overall response plot is a vector sum of these frequency components for horizontal and vertical directions, respectively, and several other sub- and superharmonic frequency components which are not shown here. The response of the nth multiple of the varying compliance frequency (VC) peaks at 1/nth of the frequency at which the VC frequency peaks.

Three regions of period 1 unstable response are seen in Figure 4. The first region from 915 to 6900 r.p.m. has period-doubling bifurcations. The eigenvalues of the monodromy matrix go out through -1. This is also a region of multivalued solutions in which it is difficult to find the different nT periodic solutions by numerical integration. Multiple solutions at a speed of 1150 r.p.m. were found by HBM as shown in Figure 6.

Three regions of chaotic behavior are seen in this region. For the first chaotic region 1780–1880 r.p.m. the loss of stability is seen to be with the eigenvector crossing from $+1$.

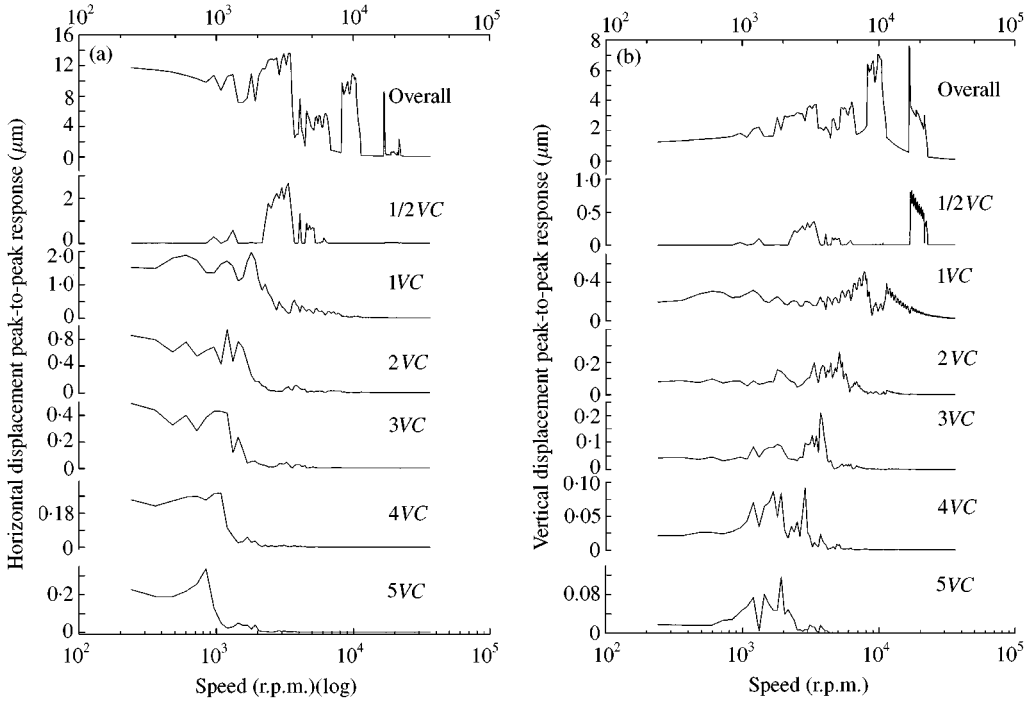

Figure 5. (a) nVC responses plots for horizontal displacement $\gamma = 20\ \mu$m, $C = 200$ N s/m; (b) nVC plots of vertical displacement, $\gamma_0 = 20\ \mu$m $C = 200$ N s/m.

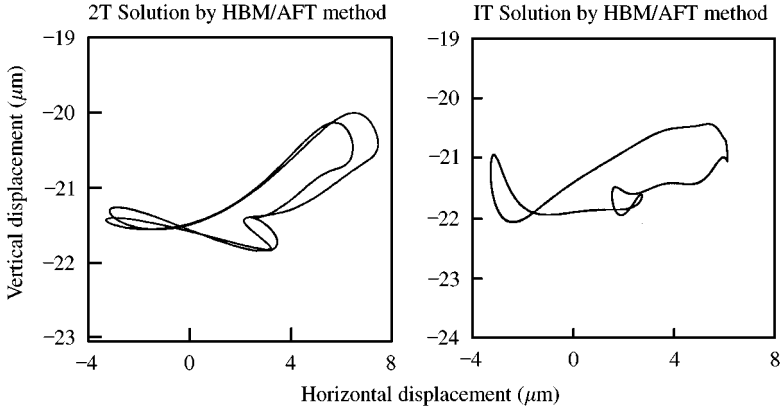

Figure 6. 1150 r.p.m.

The route to chaos by sudden loss of stability through a limit point has been shown by Sankaravelu [8]. The chaotic solution at 2120 r.p.m. is shown in Figure 7. The frequency spectrum has a band structure as shown in between spikes of VC and its multiples. The fine layered structure of the strange attractor is also clear from Poincare maps and at 2180 r.p.m. the fifth subharmonic appears.

From a speed of 2550 r.p.m. onwards stability returns and there are period-doubling bifurcations. As the speed is increased, the chaotic response appears between 5400 and

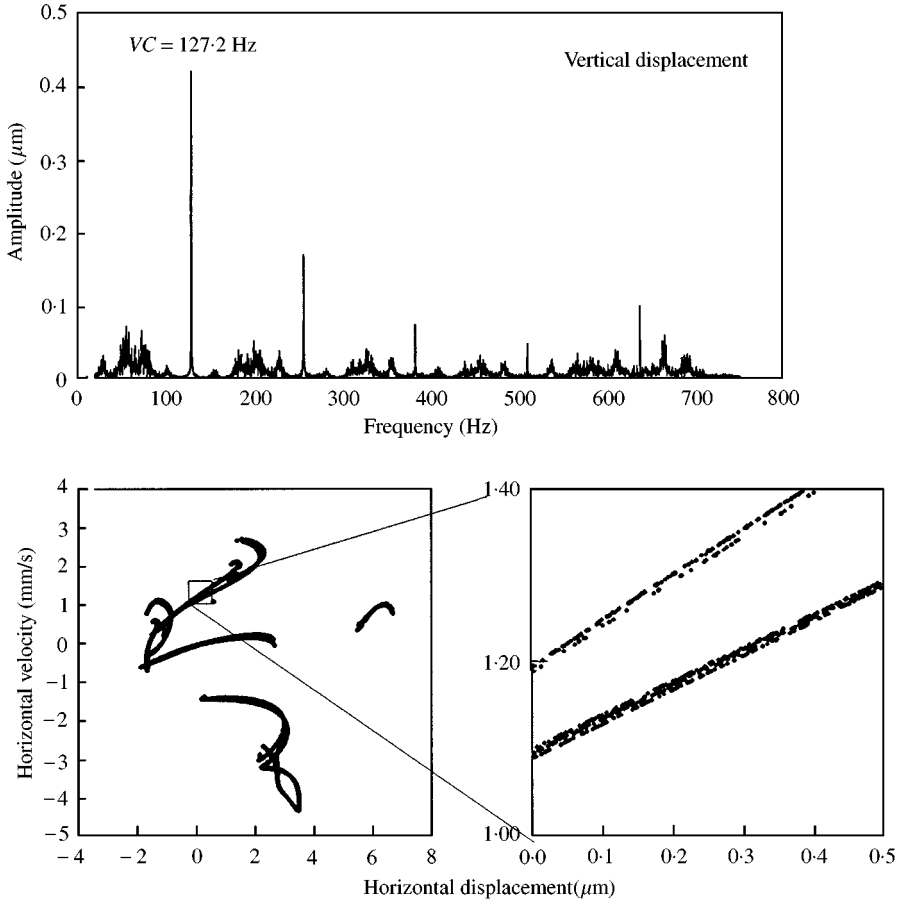

Figure 7. 2120 r.p.m., $\gamma_0 = 20$ μm, $C = 200$ N s/m.

6945 r.p.m. Below 5400 r.p.m. the response is period one unstable. Period-doubling bifurcation gives way to chaos at 5400 r.p.m. (Figure 8). The chaotic behavior in this region seems to be very strong as compared to the region between 1980 and 2550 r.p.m. The chaotic attractor is spread out and the band of frequency in the spectrum formed is also quite prominent. As the speed is increased to 5500 r.p.m., the seventh subharmonic appears after which the system again goes into period-doubling bifurcation. These pitchfork bifurcations lead to chaos at 6400 r.p.m. From Figure 9 it can be seen that the chaos at 6400 r.p.m. is through a route of pitchfork bifurcations till 6300 r.p.m. after which chaos suddenly appears. As speed increases, stability returns by a torus solution which is very clear from the Poincare map at 6850 r.p.m.

From 7600 to 9000 r.p.m. there is period one stable response. From 9000 r.p.m. again pitchfork bifurcation takes place and that leads to a chaotic region from 9715 to 10 500 r.p.m. as shown in Figure 10. In this region, the period-doubling bifurcations give way to chaos at about 9700 r.p.m. The chaotic region extends up to 10 500 r.p.m. after which the solution has a fifth subharmonic at 10 750 r.p.m. (Figure 11). The vertical displacement response has a very strong nature of the fifth subharmonic which is clear from the multiple curve phase plane plot. The phase plane plot for horizontal displacement does not show the presence of any subharmonic.

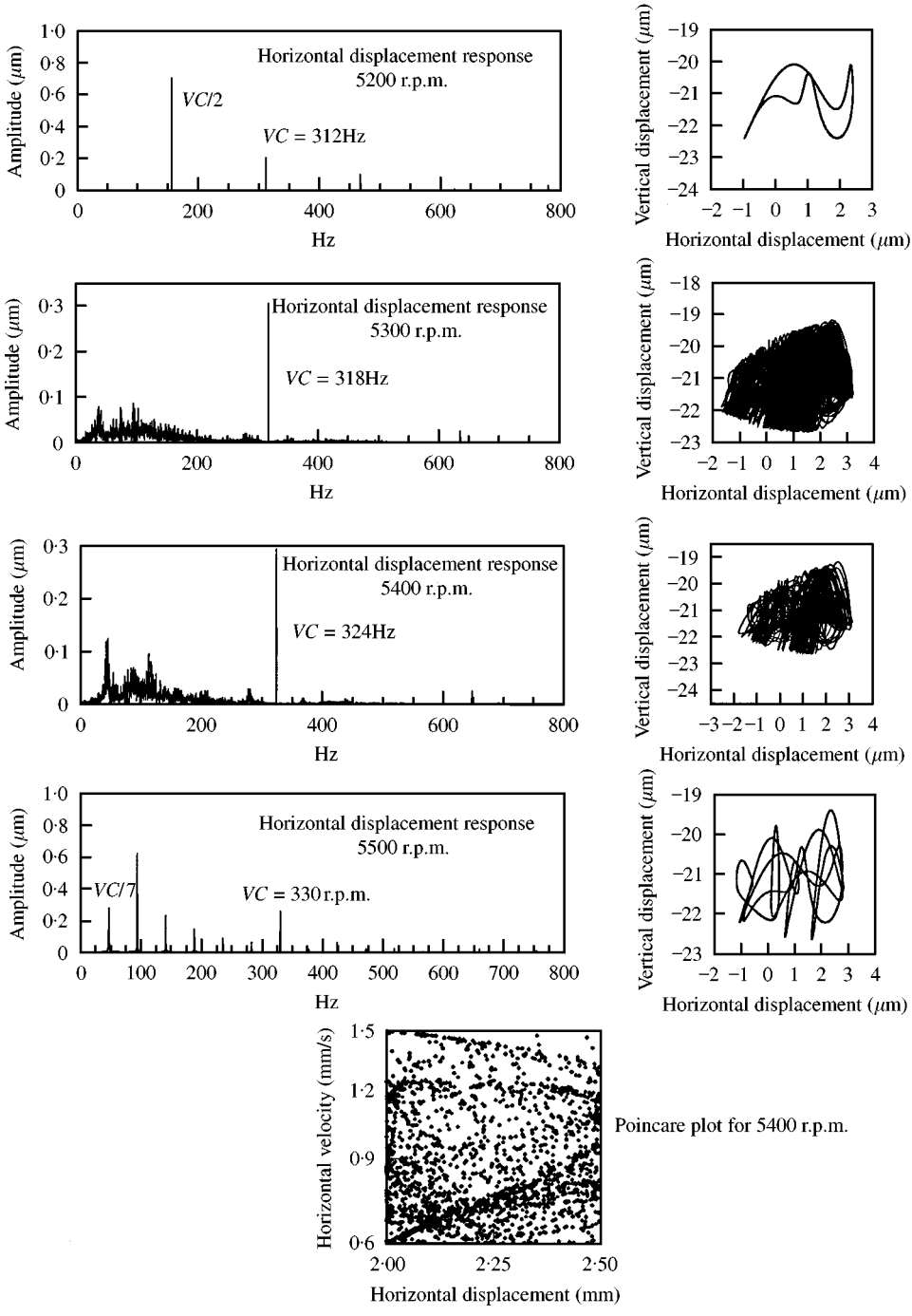

Figure 8. 5400 r.p.m., $\gamma_0 = 20$ μm, $C = 200$ N s/m.

Fukata [4], Mevel and Guyader [5] have reported period one unstable behavior or chaos around the vertical and horizontal critical speeds. In this study, one observes that large clearance results in very wide unstable regions which are not necessarily around the critical speeds. From 17 000 to 22 500 r.p.m. again, there is period one unstable behavior. This

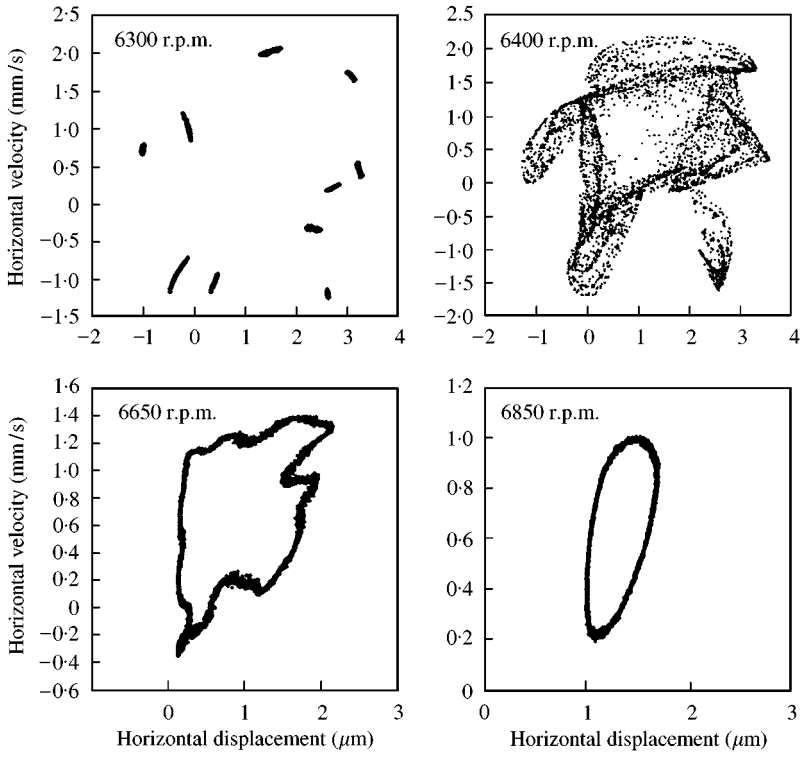

Figure 9. 6400 r.p.m., $\gamma_0 = 20\ \mu$m, $C = 200$ N s/m.

(third) region C–C′ is not reported by Fukata [4], Mevel and Guyader [5] or Sankaravelu [6], since they have not taken clearance as a parameter of study, so this region could not be studied by them. At 17 000 r.p.m. the eigenvalues of the monodromy matrix indicate Hopf bifurcation.

6.2.2. $\gamma_0 = 20\ \mu m\ C = 340\ N\ s/m$

On increasing the damping the level of the response peaks goes down. This is clear from a comparison of Figures 4 and 12. Though the three regions of unstable behavior remain, they reduce in terms of the range of speed. For a speed of 1630 r.p.m., the solution from numerical integration compares well with the HBM solution (Figure 13). The period one solution by way of pitchfork bifurcation loses stability at 1645 r.p.m. (for 200 N s/m it is 915 r.p.m., Figure 4). This region is also multivalued and has period-doubling bifurcations. At 8500 r.p.m. by way of Hopf bifurcation the solution becomes unstable. It is seen that the frequency generated due to Hopf bifurcation changes with speed. The ratio between VC frequency (carrier frequency) and modulating frequency given by p decreases as speed increases (Figure 12). The torus solution becomes an IT stable solution at 10 750 r.p.m. The Poincare map in Figures 14(a) and 14(b) show the nature of solution is torus and IT stable. In Figure 14(b), the point becomes a fuzzy area as the hyperplane crossing is determined for a tolerance ε (since the exact crossing is difficult to establish).

The third area of instability between 17 000 and 22 500 r.p.m. appears for the high damping case also. The peak-to-peak amplitude in this region is lower for higher damping

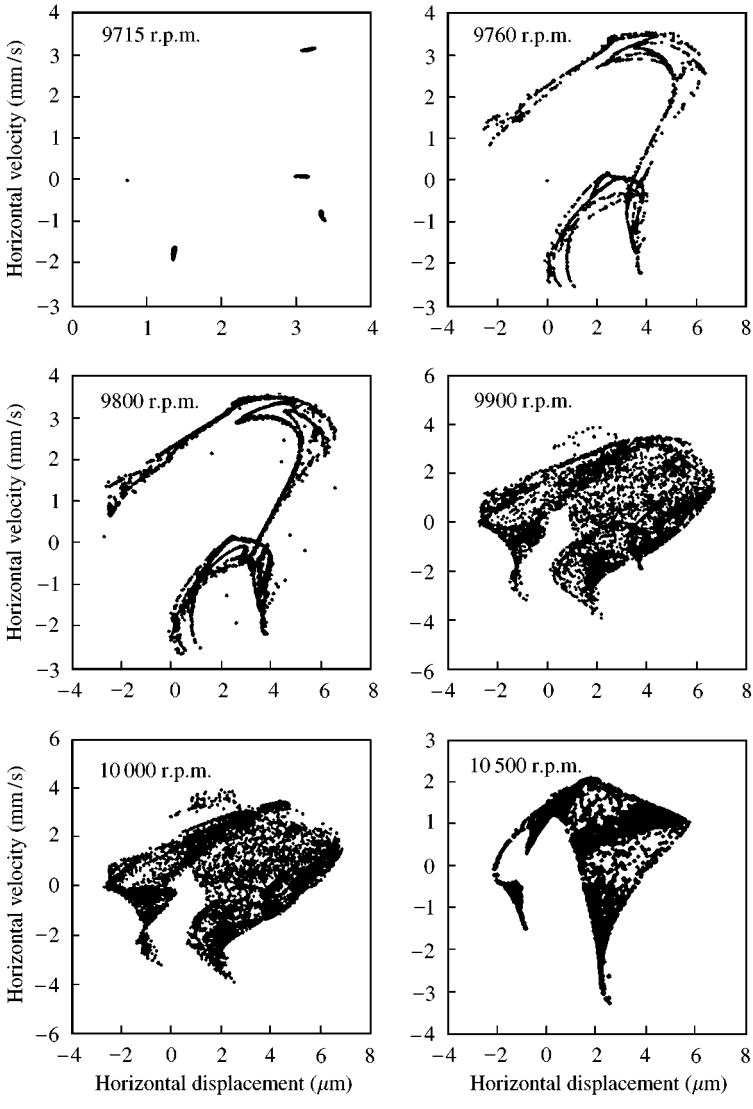

Figure 10. 9800 r.p.m., $\gamma_0 = 20$ μm, $C = 200$ N s/m.

and for horizontal displacement response this region does not develop at all. The solutions in this region are 2 T stable.

6.2.3. $\gamma_0 = 12$ μm $C = 200$ $N\,s/m$, $W = 6$ N

For an internal radial clearance of $\gamma_0 = 12$ μm the response is analyzed for two values of damping, 200 and 340 N s/m. From Tamura's [7] estimate of stiffness in the vertical and horizontal directions (Figure 3) it is seen that for $\gamma_0 = 20$ and 12 μm, the stiffness value practically remains the same in the horizontal and vertical directions. On analyzing the response plot for peak-to-peak amplitude against speed for the cases of $\gamma_0 = 20$ and 12 μm (Figures 4 and 15), it is seen that the peak (shown by P' in Figure 4) develops at a lower speed, 3500 r.p.m. for an increased radial clearance of 20 μm (Figure 15), it is at 4000 r.p.m.

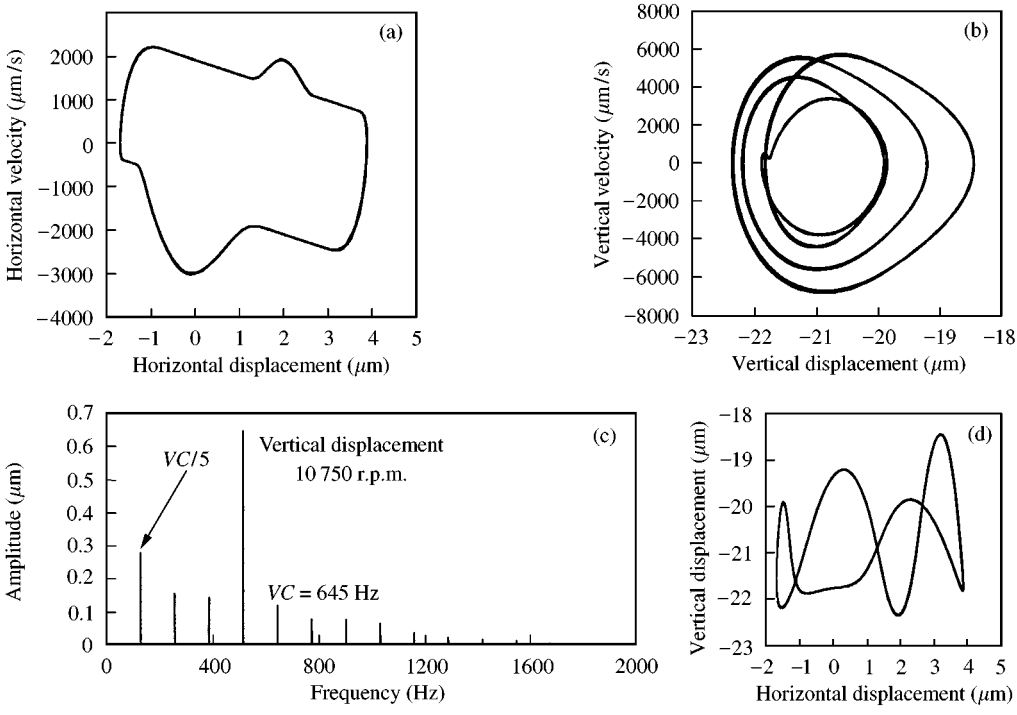

Figure 11. 10 750 r.p.m., $\gamma_0 = 20$ μm, $C = 200$ N s/m.

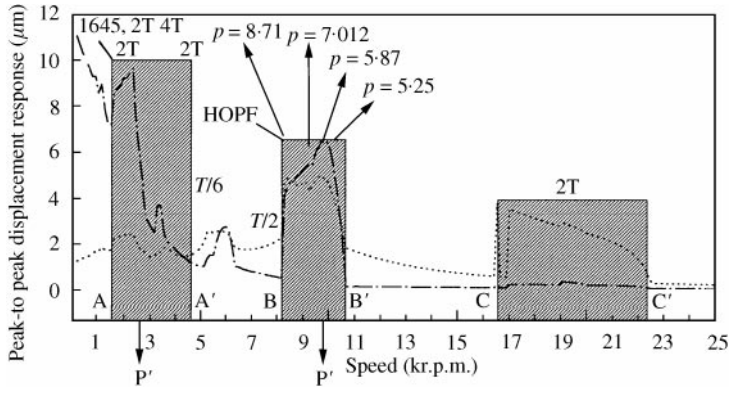

Figure 12. Response plots, $\gamma_0 = 20$ μm, $C = 340$ N s/m: ·····, vertical; – · –, horizontal; ▨, period one unstable.

The region BB′ for 20 μm clearance (Figure 4) has peak at 10 000 r.p.m. whereas for 12 μm (Figure 15) it is at 12 000 r.p.m. This shift in peaks points to an increase in the value of stiffness as clearance decreases. On comparing Figure 4 with Figure 15 it can be seen that regions A–A′, B–B′ and C–C′ (which are regions of period one instability) shift towards lower speed as clearance is increased. Within the regions A–A′ and B–B′ are the horizontal and vertical critical speeds of the system respectively. Period one solution becomes unstable from 1345 r.p.m. onwards, because of period-doubling bifurcations. The solution undergoes pitchfork bifurcations (2, 4, and 8 T) till 2400 r.p.m. after which at 2440 r.p.m. chaotic

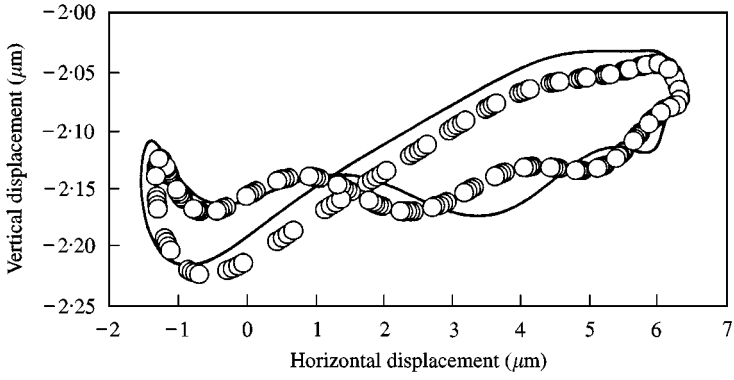

Figure 13. 1630 r.p.m., $\gamma_0 = 20$ μm, $C = 340$ N s/m: —— numerical integration; ○, HBM/AFT.

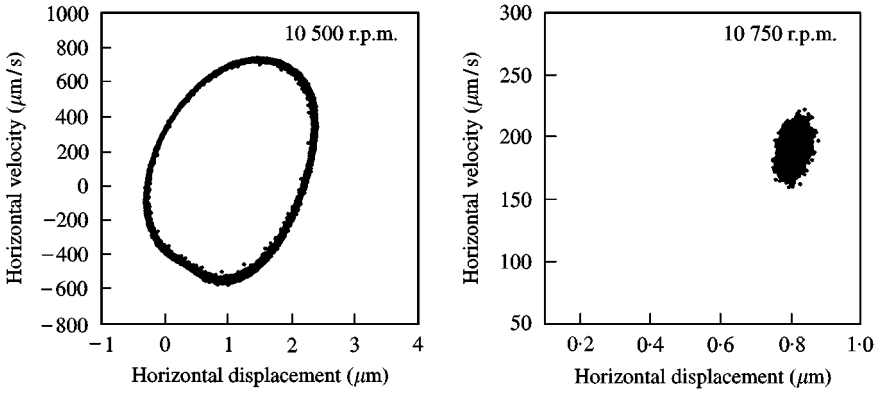

Figure 14. Poincare maps $\gamma_0 = 20$ μm, $C = 340$ N s/m.

solution is obtained. From a speed of 2400–2900 r.p.m. the response becomes chaotic. From Figure 16 at 2820 r.p.m., the band nature of the frequency spectra clearly indicates chaotic solution. The Poincare map also shows the characteristic "layered" structure of a chaotic response. From 3340 r.p.m., period one solution again becomes stable. Also, the peak-to-peak response goes down (Figure 15), which is an indication of the end of the multivalued region of response.

At a speed of 9500 r.p.m. a Hopf bifurcation occurs and again the peak-to-peak response goes up. At 9500 r.p.m. the response is mode locked with the ratio between the varying compliance frequency (570 Hz) and the newly generated frequency (71·25 Hz) being $8(= p)$. As the speed is increased the value of p decreases acquiring values of 6·09 and 5 at 11 000 and 12 000 r.p.m respectively. At 12 000 r.p.m. the solution becomes mode locked with $p = 5$. The Poincare map (Figure 17(b)) shows the period 5 orbit intersecting the hyperplane.

From 13 000 r.p.m. the response becomes IT stable with low amplitude (Figure 15). The third region CC′ starts at 20 400 r.p.m. The IT solution changes into a chaotic solution as indicated by Poincare maps in Figure 18. The strange attractor shows signs of strong chaos which begins to weaken from 20 800 r.p.m. onwards and the torus solution appears at 21 010 r.p.m. After this, a mode locked response appears. The VC/5 makes an appearance at

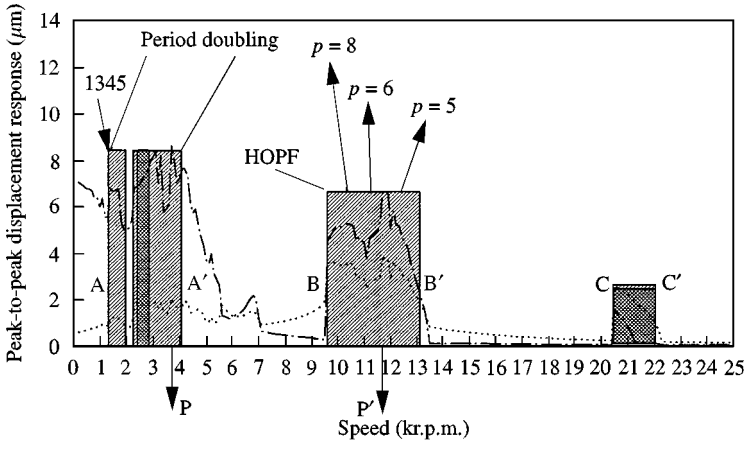

Figure 15. Response plot, $\gamma_0 = 20\ \mu$m, $C = 200$ N s/m: ·····, vertical; –·–, horizontal; ▦, chaotic response; ▨, period 1 unstable.

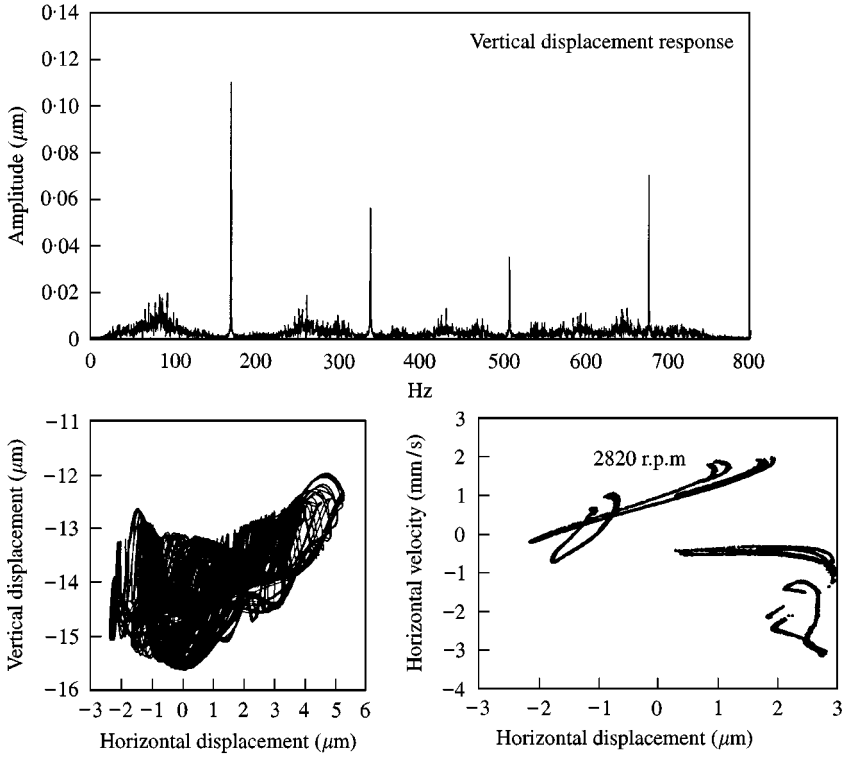

Figure 16. 2820 r.m.s., $\gamma_0 = 12\ \mu$m, $C = 200$ N s/m.

20 750 r.p.m. (Figure 19) and the mode locked response is clearly visible from the time response of the vertical displacement. The time period of the carrier frequency is 0·0085 s ($f = 125\ Hz = VC/5$). The chaotic response seems to be weakly present giving the characteristics of intermittency indicated y region AA′ of the time response plot of Figure 19.

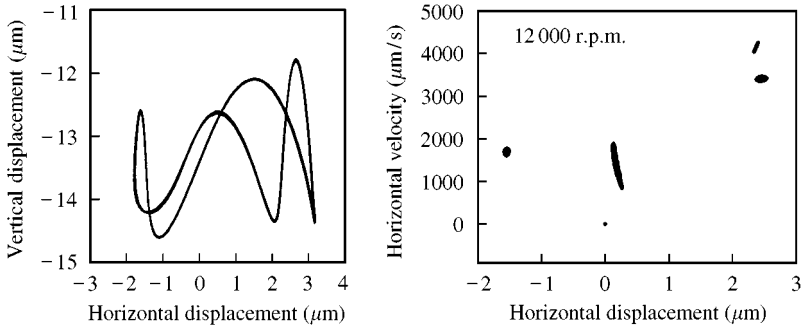

Figure 17. 12 000 r.p.m., $\gamma_0 = 12$ μm, $C = 200$ N s/m (orbit, Poincare map).

6.2.4. $\gamma_0 = 12$ μm, $C = 340$ *N s/m*, $W = 6$ *N*

On increasing damping, the peak-to-peak amplitude goes down as compared to $C = 200$ N s/m (Figure 15). The variation in the peak-to-peak amplitude as speed is increased also goes. The result is a smoother curve as shown in Figure 20(a). An important difference from the previous cases is that the third region CC′ is not present. The response plots of 1/2VC (Figures 20(b,c)) also do not show high amplitude at twice the critical speed.

Period one solution loses stability at about 2000 r.p.m. as a result of pitchfork bifurcation. The region A–A′ becomes a multivalued region. At 2100 r.p.m. the multivalued solution (Figure 21), is obtained by finding the fixed point for successive speeds, starting from a region where there is low amplitude and strong 1 T stable (single-valued solution). For the present case, it was about 1000 r.p.m. The initial value for succeeding speeds (speed step = 5 r.p.m.) was taken as a fixed point of preceding speed. For small changes in speed and other parameters remaining constant, the fixed point also remains nearly the same, but there is a gradual change in its value. To continue on the desired KT solution ($K = 1, 2, \ldots$), it is important to move like this. This procedure is repeated for decreasing speed steps (5 r.p.m.) from some higher value of speed. In this case it was taken as 2300 r.p.m. On running "backwards" and "forward" at 2100 r.p.m. different fixed points were obtained. Using these as initial conditions gave the 1 T solution (Figure 21(a)) and 4 T solution (Figure 21(b)). At 2380 r.p.m., a weak chaotic solution forms. This multivalued high peak-to-peak amplitude region gives way to stable period one solution at 4200 r.p.m..

The period one solution remains stable uptill a speed of about 9700 r.p.m. when a Hopf bifurcation takes place. The value of the new frequency which is generated because of Hopf bifurcation changes with speed in the same manner as in the other cases where the ratio between the exciting frequency and the new frequency ($= p$) decreases as speed increases (9900 r.p.m., $p = 7{\cdot}61$; 10 500 r.p.m., $p = 6{\cdot}3$; 11 000 r.p.m., $p = 5{\cdot}54$; 12 000 r.p.m., $p = 4{\cdot}77$).

6.2.5. $\gamma_0 = 6$ *μm* $C = 200$ *N s/m* $W = 6$ *N*

The speed response plot in Figure 22 has only one well-developed region of high amplitude AA′. The peak for this level of clearance develops at a higher speed (6200 r.p.m.) compared to a clearance of 12 μm (4000 r.p.m.) and 20 μm (3500 r.p.m.). This gradual shift in

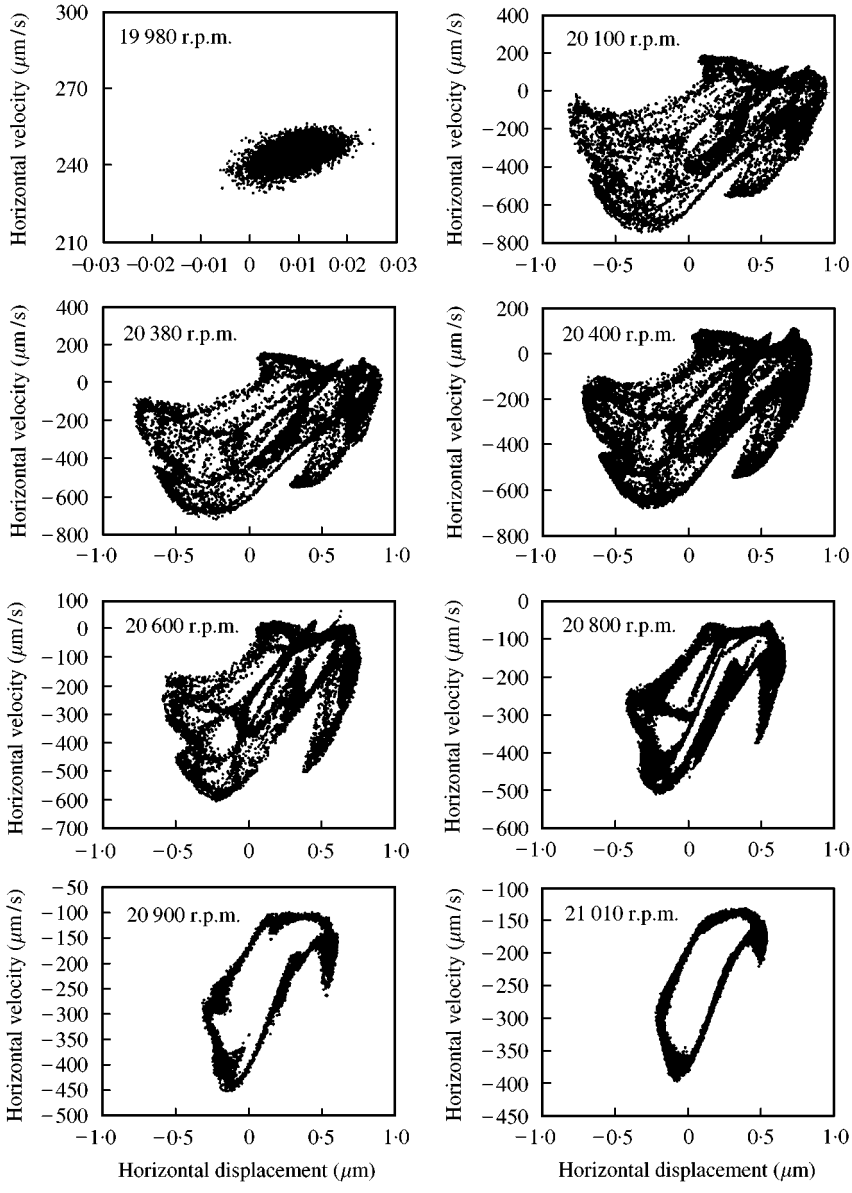

Figure 18. Poincare map (19 980–21 010 r.p.m.).

critical speed as a function of clearance is also reflected in the experimental observations. From the response plot of VC and its components for vertical displacement, it can be seen that $\frac{1}{2}$VC develops a peak at twice the critical speed, Figure 23 ($\approx$ 24 000 r.p.m.). This peak is not so well developed as compared to $\gamma_0 = 20$ μm cases. For $\gamma_0 = 6$ μm (Figure 23), the peaks smoothen out. Also, the peaks "A" shift down for higher frequency components.

Period one solution loses stability at 3200 r.p.m. by pitchfork bifurcation to 2 T solution. At 3300 r.p.m. there is a 5 T solution (Figure 24) from which at 3400 r.p.m. a chaotic solution forms. At 3500 r.p.m., 5 T solution forms which turns to 3 T at 3600 r.p.m. This

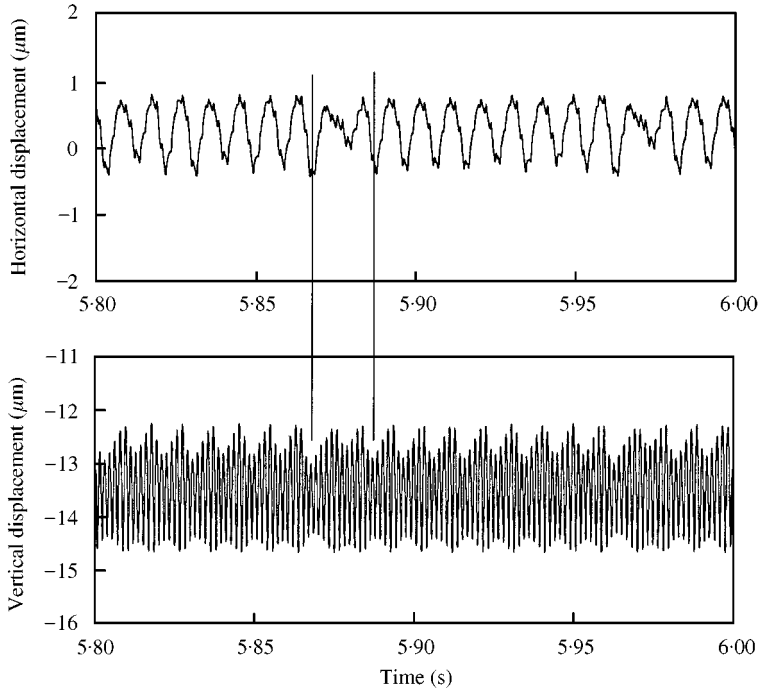

Figure 19. 20 750 r.p.m., $\gamma_0 = 12$ μm, $C = 200$ N s/m.

solution stays at 3 T till about 3800 r.p.m. when the response becomes chaotic again. The chaotic region continues till 4700 r.p.m. Then the response becomes a 2 T solution that remains till 7000 r.p.m. after which the high peak-to-peak amplitude, multivalued region again regains 1 T stable solution and low amplitude which continues up to 10 500 r.p.m. At speeds higher than this, the increase in amplitude is much smoother with no signs of instability. The amplitude, however, increases and peaks at 11 200 r.p.m. and then starts reducing till 14 000 r.p.m. This smooth behavior resembles the response of a linear system. The reduced internal radial clearance of 6 μm obviously reduces the degree of non-linearity and results in this linear "tendency" of the system. Noticeably, the peak attained at 11 500 r.p.m. appears only for vertical displacement response, the horizontal displacement does not develop a peak. Qualitatively, this shows the absence of cross-coupling stiffness in the vertical direction. In the horizontal direction, there is some coupling as horizontal and vertical displacement peaks at around 6500 r.p.m. The weak cross-coupling stiffness also results in the absence of Hopf bifurcation for this clearance and damping value. Day [14] has shown analytically that Hopf bifurcation depends directly on the ratio of cross-coupling stiffness with damping of a rotor supported on bearings with radial internal clearance.

At 14 500 r.p.m., a weak superharmonic resonance is noticed. In a very short speed range of 23 000–23 400 r.p.m. another small peak forms. This peak develops only for the vertical displacement response and the nature of solution is 2 T.

6.2.6. $\gamma_0 = 6$ μm, $C = 340$ $N\,s/m$, $W = 6$ N

Speed response characteristics for this case are given in Figure 25. Only one region of instability beginning from 4000 r.p.m. is identified. Period one stable solution loses stability

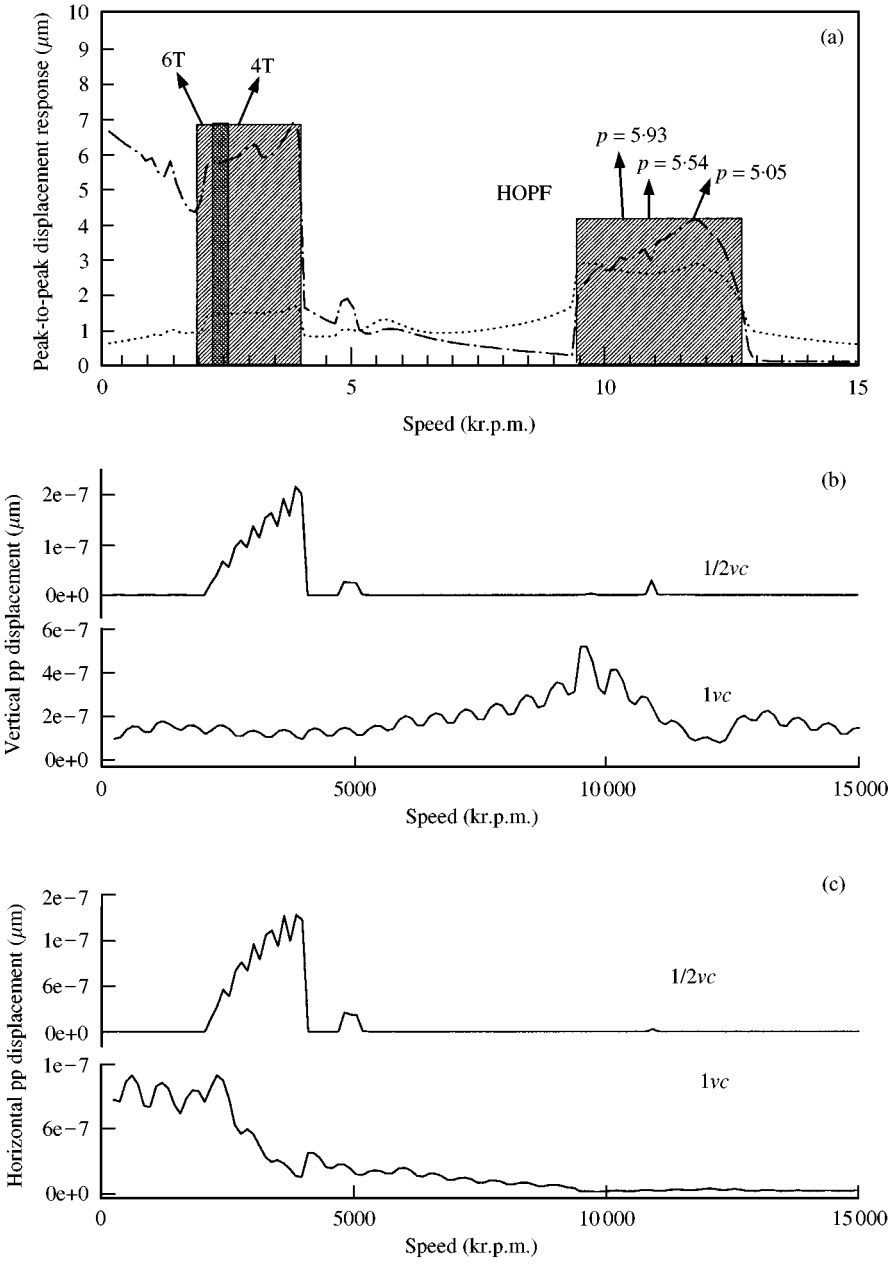

Figure 20. Response and nVC plots, $\gamma_0 = 12\ \mu$m, $C = 340$ N s/m: · · · · · ·, vertical; – · –, horizontal.

at 4000 r.p.m. by period-doubling bifurcations. The region of period one unstable solutions has 2 T behavior till 7000 r.p.m.

6.2.7. $\gamma_0 = 1\ \mu m$, $C = 200$ *and* $340\ N\ s/m$, $W = 6\ N$

For a clearance value of 1 μm the response plot, Figure 26, displays a strong resemblance to the response plots of a linear rotor-bearing system with parametric effect [19]. The peaks

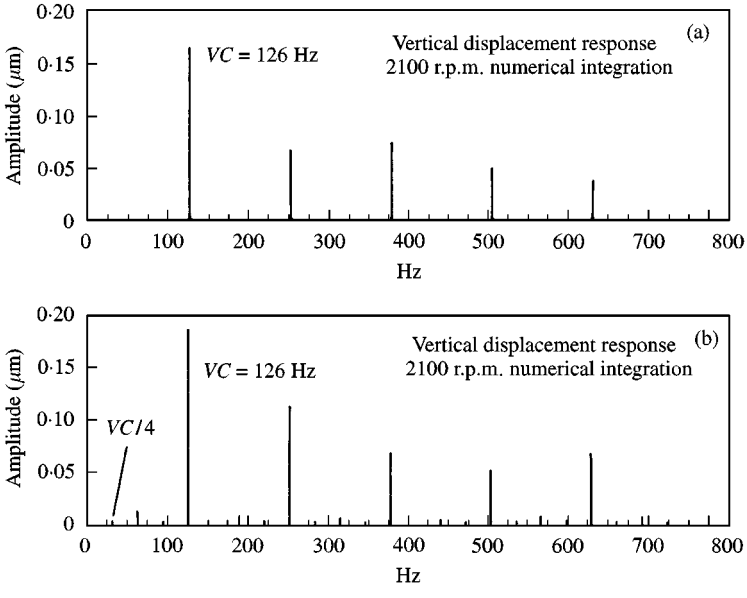

Figure 21. 2100 r.p.m., $\gamma_0 = 12\ \mu$m, $C = 340$ N s/m.

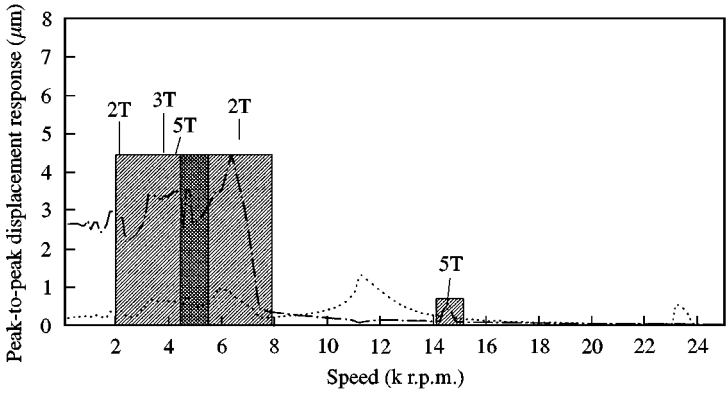

Figure 22. Response plot, $\gamma_0 = 6\ \mu$m, $C = 200$ N s/m: · · · · ·, vertical; – · –, horizontal; ▨, unstable period 1 solution; ▦, chaotic response.

develop at subsynchronous speeds which are 1/2, 1/3, 1/4, … of the critical speed in the vertical and horizontal directions. This is very clearly observed from Figure 25 where VC, 2VC, 3VC, 4VC, 5VC peak exactly at 1/2, 1/3, 1/4, 1/5 of the critical speed in the horizontal and vertical directions. But there is no peak formed in the supersynchronous region unlike the cases of $\gamma_0 = 20$, 12 and 6 μm. As a result, 1/2 VC component does not develop a peak at twice the critical speed. There are no regions of period 1 unstable solution. The regions of high amplitude have superharmonic motion.

6.2.8. $W = 24\ N$

The vertical and horizontal critical speeds for $W = 24$ N are 15 800 r.p.m. and 5000 r.p.m. respectively (Figure 3). For an increase in the constant radial force W the regions of period

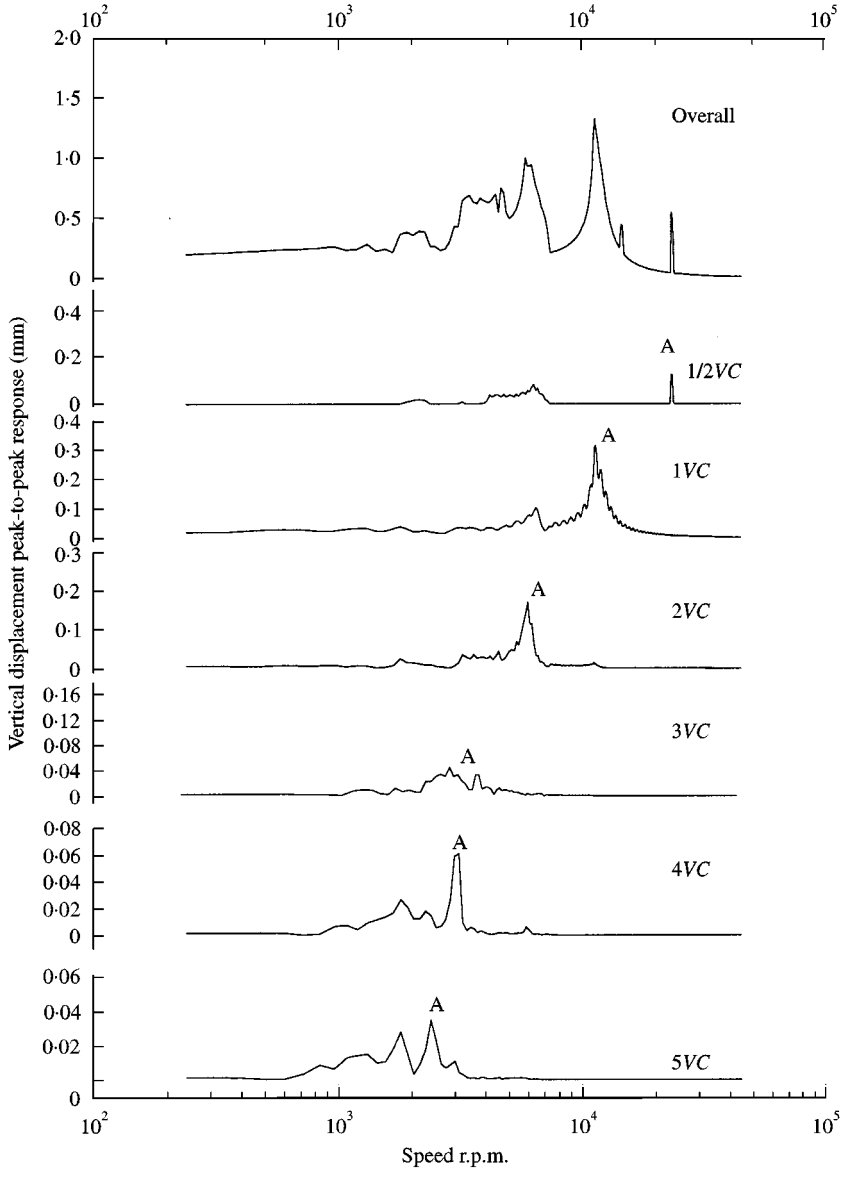

Figure 23. nVC vertical displacement plot $\gamma_0 = 6\ \mu$m, $C = 200$ N s/m.

one instability decrease as shown in Figure 27, in which there are only two regions as compared to three regions for $W = 6$ N (Figure 4) and also the regions of chaos. For $\gamma_0 = 20\ \mu$m $C = 200$ N s/m, Figure 27, at 13 100 r.p.m., there is a Hopf bifurcation and the response solution again becomes high amplitude. The torus solution gives way to chaotic solution at 15 000 r.p.m. (Figure 28). This chaotic solution is present for a very short speed span till 16 000 r.p.m. The chaotic solution weakens to give way to a torus solution at 15 500 r.p.m. The phase plane plots show the existence of two limit cycles which coexist, one is bigger and the other which is smaller but dense (Figure 29).

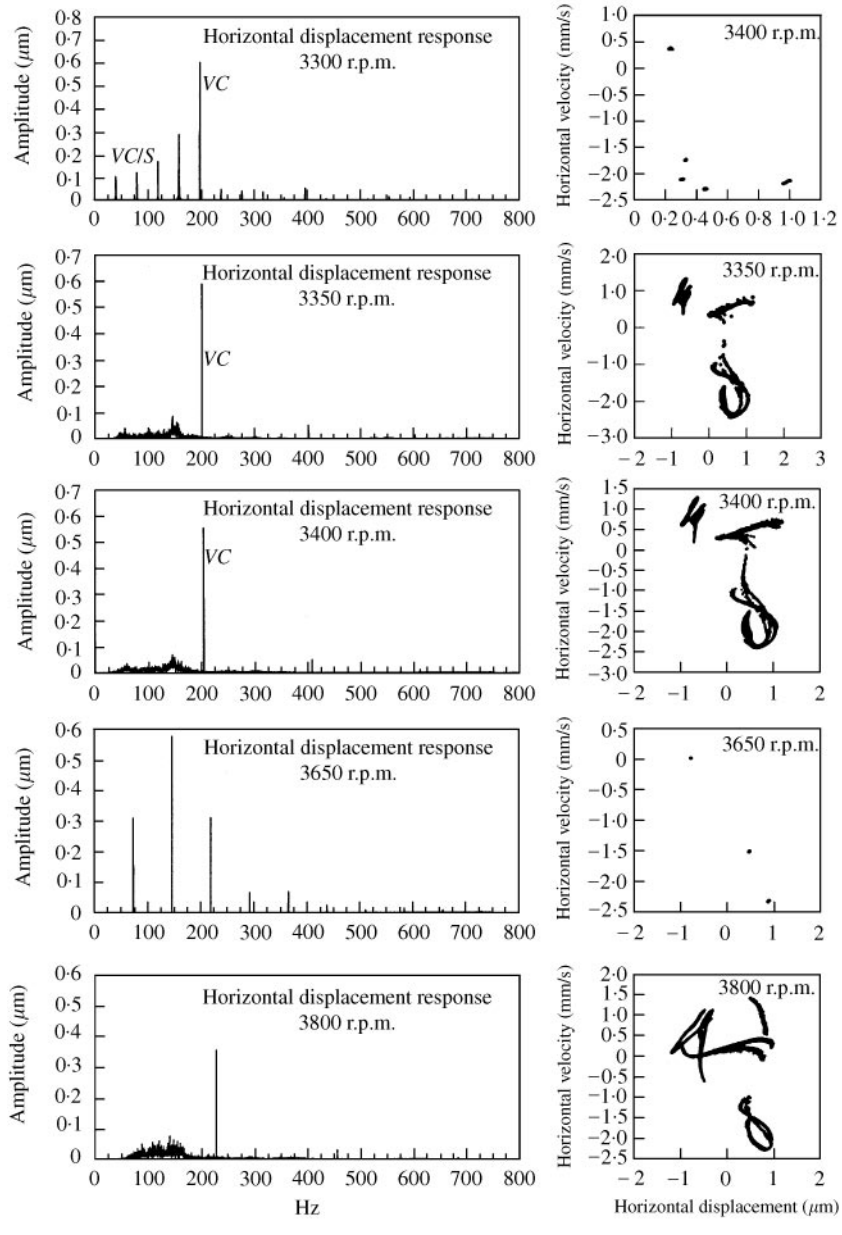

Figure 24. Poincare maps (3300–3800 r.p.m.).

7. EXPERIMENTAL INVESTIGATION

A experimental setup is used for studying the effect of bearing radial internal clearance on the dynamic response of the rotor (Figure 30). The signals are obtained with the help of proximity probes in the horizontal and vertical directions. These two signals are input into a dual channel spectrum analyzer (DSA)HP 3582A. The setup has been made so that we have a horizontal Jeffcott rotor supported on anisotropic bearings. In this case, the displacement response in the horizontal and vertical directions would peak at different speeds corresponding to the bearing stiffness in the two directions [19].

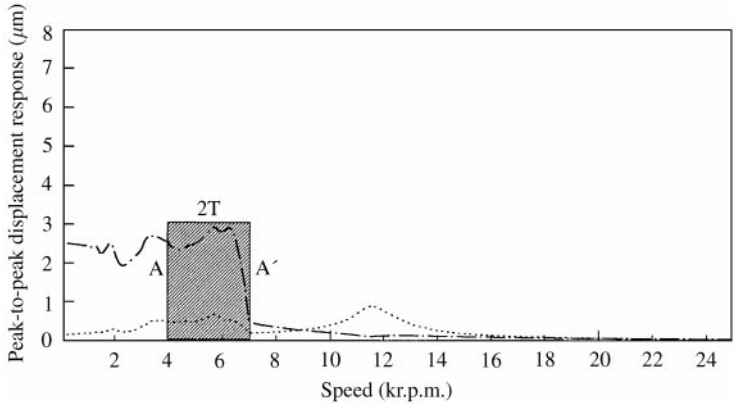

Figure 25. Response plot, $\gamma_0 = 6\ \mu$m, $C = 340$ N s/m: · · · ·, vertical; –·–, horizontal; ▨, unstable period 1 solution; ▦, chaotic response.

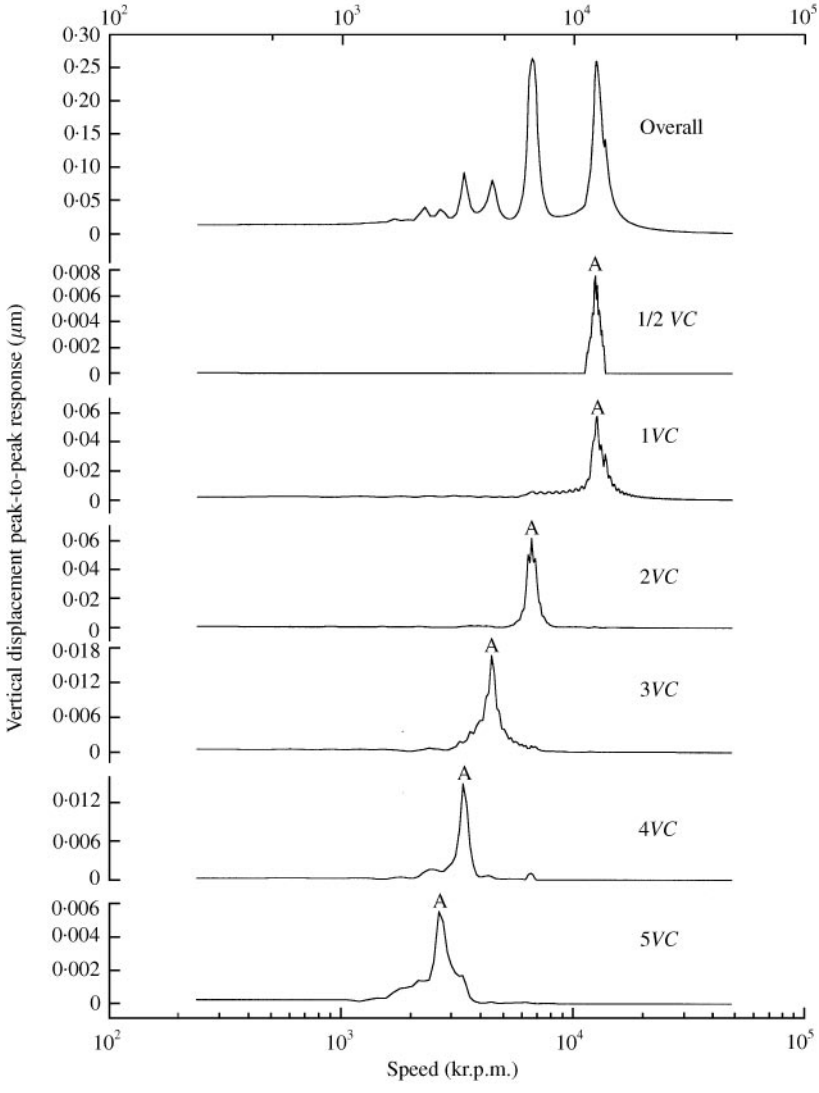

Figure 26. nVC vertical displacement response plots, $\gamma_0 = 1\ \mu$m, $C = 200$ N s/m.

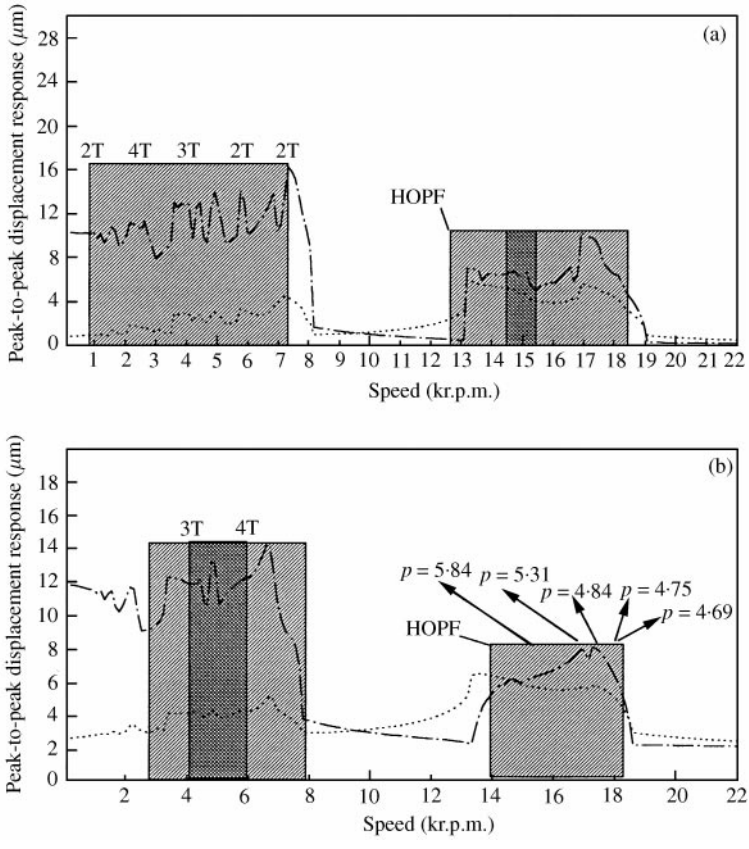

Figure 27. Response plot, $W = 24$ N, $\gamma_0 = 20$ μm. (a) $C = 200$ N s/m: · · · · ·, vertical; – · –, horizontal; ▨, unstable period one solution; ▦, chaotic response; (b) $C = 340$ N s/m: – · –, horizontal; · · · · ·, vertical; ▨, unstable period one response; ▦, chaotic solution.

The rotor system is horizontal and this results in the appearance of a very strong $2X$ component in the response spectrum primarily because of clearance and anisotropic stiffness. Also, there are appearances of higher harmonics [$3X$, 4X, …] which are again the result of the clearance and anisotropic effect. It is observed from the DSA that the amplitude of $2X$ and higher harmonics peak at two frequencies. These two frequencies give us an estimate of the two natural frequencies corresponding to the stiffness in the vertical and horizontal directions.

The limitation with the present experimental setup is that the maximum attainable speed is 10 000 r.p.m. and the critical speed corresponding to bearing stiffness does not fall in this speed span. The shaft is rigid with its first flexible natural frequency above 900 Hz. Assuming that the ends of the shaft supported by ball bearings are simple supports allowing rotation, the shaft bending stiffness is given by

$$K_s = 48EI/l^3,$$

where

$$I = \pi d^4/64.$$

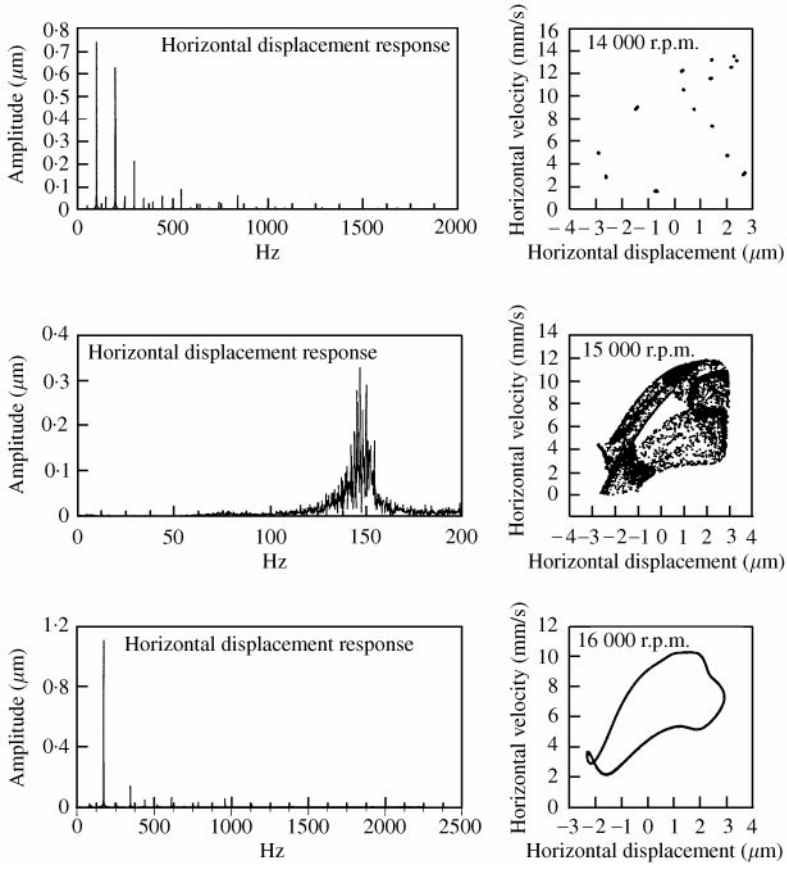

Figure 28. Frequency spectra, Poincare maps $W = 24$ N, $\gamma_0 = 20$ μm, $C = 200$ N s/m.

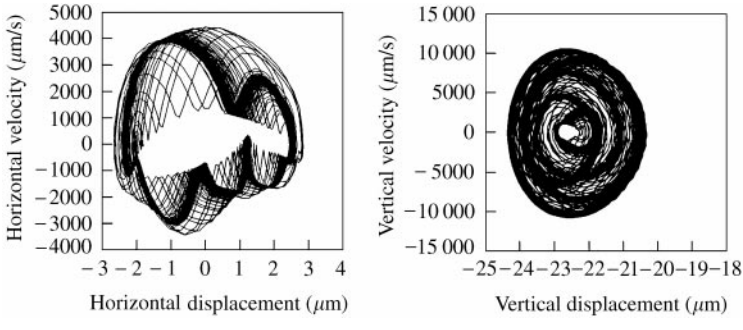

Figure 29. Phase plane plot, 15 500 r.p.m.

Taking $l = 0{\cdot}06$ m, $r = 0{\cdot}076$ m, $E = 2{\cdot}0 \times 10^{11}$ N/m^2, $d = 0{\cdot}015$ m, the value of $K_s = 1{\cdot}6 \times 10^8$ N/m.

The bearing stiffness as found out theoretically from Tamura's [7] and Gargiulo's [8] methods is of the order of 10^7 N/m. Therefore, a shaft with a stiffness of $1{\cdot}6 \times 10^8$ N/m can

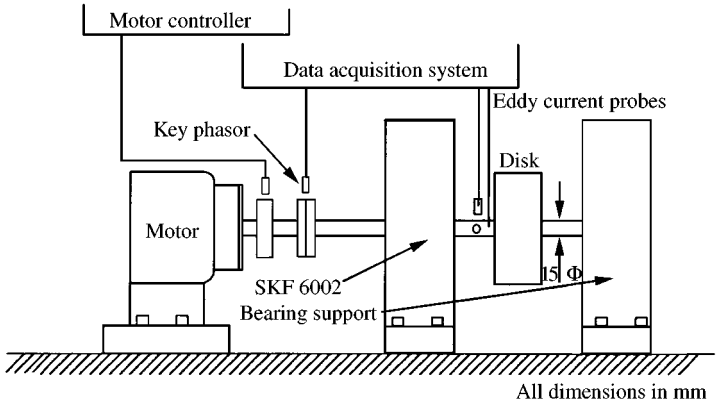

Figure 30. Experimental rig.

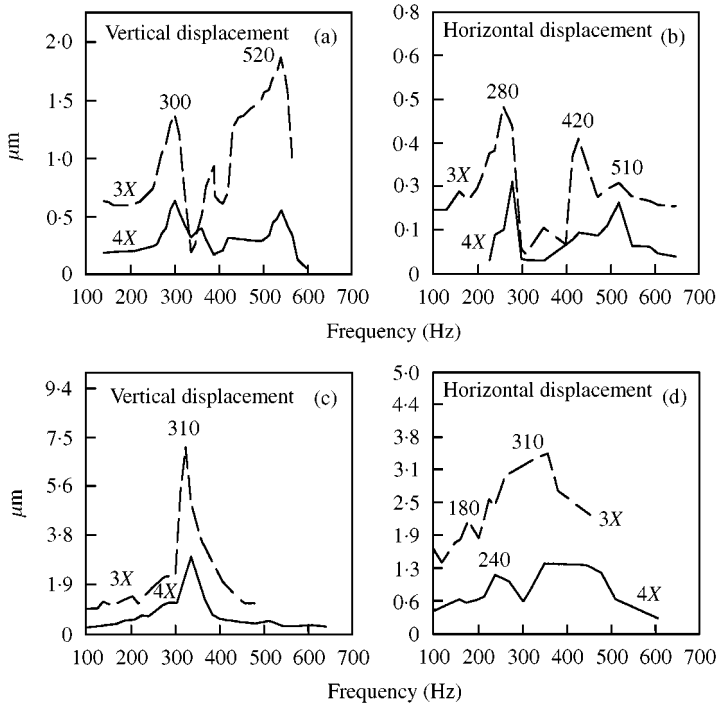

Figure 31. Response plots for $3X$ and $4X$ frequency components (a) C2 (b) C2 (c) C5 and C5-type SKF6002.

be taken as rigid. The rotor is run from 0 to 10 000 r.p.m. and the vertical and horizontal displacement responses are fed into the DSA. The $3X$ and $4X$ frequency components are tracked and at various speeds the averaged r.m.s. amplitude is noted. The r.m.s. averaging is done at a number of steady state speeds for 64 samples. This is done for the shaft supported on C2 and C5 bearings as two separate setups. The observations have been plotted and displayed in Figures 31(a–d).

TABLE 2

Critical frequency for SKF6002

	Lower peak (Hz)	Higher peak (Hz)
C2	280–300	420–510
C5	180–210	330–420
Shift in critical frequency from C2 to C5 (For change in bearing type)	~ 100	~ 100

From Figures 31(a,b) for C2-type bearing (bearing of smaller clearance of about 5 μm), the amplitudes of $3X$ and $4X$ peaks are at two frequencies, i.e., 300 and 520 Hz for the vertical direction and 280 and 420 Hz for the horizontal direction. The vertical displacement amplitude (Figure 31(a)) of both the frequency peaks is more than the horizontal displacement amplitude (Figure 31(b)). The vertical displacement signals for both the frequency peaks ($3X$ and $4X$) coincide very well at 300 and 520 Hz. For the horizontal displacement signal, the frequency peaks ($3X$ and $4X$) do not coincide very well. The higher peak for $3X$ is at 420 Hz and for $4X$ about 500 Hz. There seems to be better matching for the lower peak at 280 Hz. The mismatch at higher frequency is difficult to explain. It may, however, be due to the presence of some coupling between horizontal and vertical modes in the case of $4X$ component. For the vertical displacement signal (Figure 31(a)), the higher frequency peak is the larger of the two because this frequency corresponds to the critical speed due to the vertical stiffness. Similarly, in Figure 31(b) for the horizontal displacement signal, the lower peak is the larger of the two since this is the critical frequency for the horizontal stiffness.

For C5-type bearing (higher clearance of about 40 μm), from Figures 31(c,d) the peaks appear at 310 Hz for vertical displacement and at around 400 Hz for horizontal displacement. In Figure 31(c) the higher peak coincides at 310 Hz for both $3X$ and $4X$. The lower peak is not visible here except slightly in $3X$ at about 200 Hz. For both $3X$ and $4X$ frequency components, there is a steep rise before the peak of 310 Hz. The horizontal displacement response (Figure 31(d)) for C5 does not have very good coincidence of peaks. The lower peak appears to develop slightly around 180–240 Hz. The higher peak, which is the dominant of the two but not sharp enough appears around 330–420 Hz. The above results have been summarized in Table 2.

The lower and higher critical frequencies give an estimate of the stiffness in the Y (horizontal) and X (vertical) directions, respectively, for a given mass, i.e., 0·6 kg in the present case. The ratio between the two frequencies is about 0·6 which agrees reasonably with the value suggested by Kramer [19, p. 136]. It has been noted in the theoretical analysis of the bearing model without imbalance that under dynamic conditions because of the difference in the radial internal clearance there is a shift in critical speed. A similar trend is also shown experimentally by Flowers and Wu [17] where an increase in clearance at the rotor support shifts the critical speed down.

The horizontal and vertical stiffness work out to be $1{\cdot}9 \times 10^{\cdot 6}$ and 5×10^6 N/m for C2-type bearing and, 9×10^5 and 3×10^6 N/m for C5-type bearing.

8. CONCLUSIONS

From the study of the dynamic response of a ball bearing supporting a horizontal rigid perfectly balanced rotor the following conclusions can be drawn.

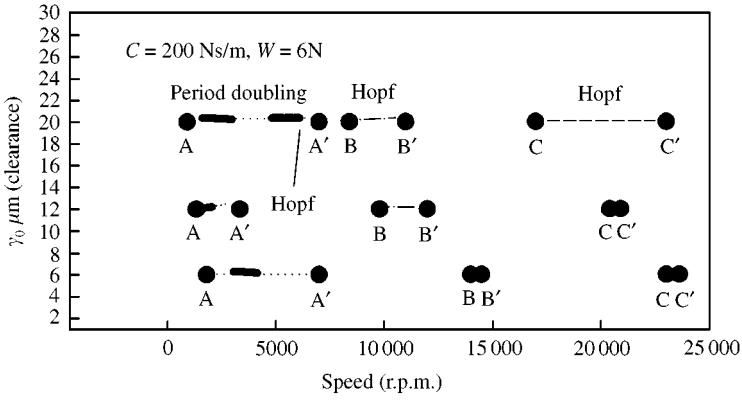

Figure 32. Regions of instability and chaotic behavior; ———, chaotic response.

TABLE 3

Shift of peaks and unstable region with clearance

	Span/peak (r.p.m.)			
Regions	20 μm	12 μm	6 μm	1 μm
A–A′	915–6800/3300	1345–3900/3700	3200–7000/6400	— /6000
B–B′	8100–11 400/10 000	9700–13 000/12 000	10 500–13 000/11 200	— /12 500
C–C′	16 700–22 200/17 000	20 200–22 000/20 200	23 000–23 800/23 200	—/—

1. The rotor bearing system has three high-amplitude regions (Figure 32). The first region is one of period-doubling response where the period one response is unstable. This region also has bifurcations leading to 3, 5 and 7 T solutions. Chaotic response appears in this region which has a weak attractor as compared to chaotic behavior in the other two regions. As Fukata [4] has shown, this region forms around horizontal critical speed.
2. The second region has unstable response due to Hopf bifurcation generating amplitude modulation and quasiperiodic response. The ratio of the carrier frequency (VC) to the modulating frequency decreases as the speed is increased. This leads to quasiperiodic and mode locked behavior.
3. The third region appears for high radial internal clearance which previous studies have not predicted. This region develops as a result of the peak formed due to the $\frac{1}{2}$ VC frequency component in the horizontal and vertical directions.
4. Radial internal clearance is an important parameter for determining the dynamic response as it is seen that with increase in clearance the regions of unstable and chaotic response become wider (Figure 32, Table 3).
5. The peaks developed shift down with increase in clearance (Table 3) which points to a decrease in the dynamic stiffness of the bearing with increasing clearance. This is not predicted by the stiffness estimates provided by Tamura [7] and Gargiulo [8].
6. Decrease in clearance increases the linear characteristics of the system. There are no subharmonics formed or chaos as clearance decreases. This also happens when the constant radial force W is increased. The regions of unstable behavior decrease with increasing load. The increased load also results in higher stiffness characteristics because of the non-linear nature of the force deformation relationship.

7. Increased damping results in lowered amplitude response and also reduced instability.
8. The experimental analysis shows that bearing clearance changes the response of a rotor significantly because of the change in dynamic stiffness of the bearing. This has been shown by theoretical analysis also, although most estimates of bearing stiffness do not take into account the change in dynamic stiffness due to clearance, for example Tamura [7], Gargiulo [8].

REFERENCES

1. H. PERRET 1950 *Werkstatt und Betrieb* **3**, 354–358. Elastiche Spielschwingungen Konstant Belaster Walzlger.
2. E. MELDAU 1951 *Werkstatt und Betrieb* **7**, 308–313. Die Bewegung der Achse von walzlagern bei geringen Drehzahlen.
3. C. S. SUNNERSJO 1978 *Journal of Sound and Vibration* **58**, 363–373. Varying compliance vibrations of rolling bearings.
4. S. FUKATA, E. H. GAD, T. KONDOU, T. AYABE and H. TAMURA 1985 *Bulletin of the JSME* **28**, 899–904. On the radial vibrations of ball bearings (computer simulation).
5. B. MEVEL and J. L. GUYADER 1993 *Journal of Sound and Vibration* **162**, 471–487. Routes to chaos in ball bearings.
6. A. SANKARAVELU, S. T. NOAH and C. P. BURGER 1994 *Nonlinear and Stochastic Dynamics* AMD-Vol. 192/DE-Vol. 78, ASME, pp. 313–325. Bifurcation and chaos in ball bearings.
7. H. TAMURA and Y. TSUDA 1985 *Bulletin of the JSME* **28**, 1240–1246. On the static running accuracy of ball bearings.
8. E. P. GARGIULO 1980 *Machine Design* **52**, 107–110. A simple way to estimate bearing stiffness.
9. T. YAMAMOTO 1955 *Transactions of the JSME* **21**, 182–192. On the vibration of a shaft supported by bearings having radial clearances.
10. D. W. CHILDS 1982 *Transactions of the ASME Journal of Engineering Power* **104**, 533–536. Fractional frequency rotor motion due to clearance effects.
11. S. SAITO 1985 *Transactions of ASME, Journal of Vibration, Acoustics, Stress, and Reliability in Design* **107**, 416–420. Calculation of nonlinear unbalance response of horizontal Jeffcott rotors supported by ball bearings with radial clearances.
12. D. W. CHILDS and D. S. MOYER 1985 *Journal of Engineering for Gas Turbines and Power* **107**, 152–159. Vibration characteristics of the HPOTP (high pressure oxygen turbopump) of the SSME (space shuttle main engine).
13. R. F. BEATTY and M. J. HINE 1989 *Journal of Vibrations, Acoustics, Stress and Reliability in Design* **111**, 163–169. Improved rotor response of the uprated high pressure oxygen turbopump for the space shuttle main engine.
14. W. B. DAY 1987 *Quarterly of Applied Mathematics* **XLIV**, 779–792. Asymptotic expansions in nonlinear rotordynamics.
15. Y. B. KIM and S. T. NOAH 1990 *Nonlinear Dynamics* **1**, 221–241. Bifurcation analysis for a modified Jeffcott rotor with bearing clearances.
16. F. F. EHRICH 1992 *Journal of Vibration and Acoustic* **114**, 93–100. Observation of subcritical superharmonic and chaotic response in rotordynamics.
17. G. T. FLOWERS and FANG SHENG WU 1993 *Journal of Engineering for Gas Turbine* **115**, 279–286. A study of the influence of bearing clearance on lateral coupled shaft/disk rotordynamics.
18. Y. B. KIM and S. T. NOAH 1996 *Journal of Sound and Vibration* **190**, 239–253. Quasiperiodic response and stability analysis for a nonlinear Jeffcott rotor.
19. ERWIN KRÄMER 1993 *Dynamics of Rotors and Foundations*. New York: Springer-Verlag.
20. T. A. HARRIS 1984 *Rolling Bearing Analysis*. New York: John Wiley and Sons.
21. R. J. COMPARIN and R. SINGH 1989 *Journal of Sound and Vibration* **134**, 259–290. Nonlinear frequency response characteristics of an impact pair.
22. W. H. PRESS, S. A. TEUKOLSKY, W. T. VELLERING and B. P. FLANNERY 1992 *Numerical Recipes in FORTRAN the Art of Scientific Computing*. Cambridge, MA: Cambridge University Press, second edition.
23. T. M. CAMERON and J. H. GRIFFIN 1989 *Journal of Applied Mechanics* **56**, 149–154. An alternating frequency/time domain method for calculating the steady state response of nonlinear dynamic systems.

24. L. O. CHUA and AKIO USHIDA 1981 *IEEE Transactions on Circuits and Systems* **CAS-28**, 953–971. Algorithms for computing almost periodic steady state response of nonlinear systems to multiple input frequencies.
25. AKIO USHIDA and L. O. CHUA 1984 *IEEE Transactions of Circuits and Systems* **CAS-31**, 666–678. Frequency domain analysis of nonlinear circuits driven by multi-tone signals.
26. M. TIWARI, K. GUPTA and O. PRAKASH *Proceedings of ISROMAC*-7, 22–26 *February* 1998, *Hawaii, U.S.A.* Vol. B. 960–970. Nonlinear dynamic analysis of a rigid rotor supported on a deep groove ball bearing.
27. J. M. T. THOMPSON and H. B. STEWART 1986 *Dynamics and Chaos—Geometrical methods for Engineers and Scientists*. New York: John Wiley and Sons.
28. ALI H. NAYFEH and BALAKUMAR BALACHANDRAN 1994 *Applied Nonlinear Dynamics Analytical, Computational, and Experimental Methods*. New York: John Wiley and Sons Inc.

APPENDIX A: NOMENCLATURE

ω_{cage}	rotational speed of bearing cage, rad/s
ω_{ROTOR}	rotational speed of rotor, rad/s
ω_{vc}	varying compliance frequency, rad/s
γ_0	radial internal clearance, μm
θ_i	angular position of the ith ball in the ball bearing
Θ	dimensionless number $\gamma_0/(W/N_bC_b)^{2/3}$
ε	very small number
v_{ij}	$(i\omega_{ROTOR} + j\omega_{vc})$, i and j are integers
R_i	radius of inner bearing race
R_O	radius of outer bearing race
N_b	number of bearing balls
BN	bearing number, $R_i/(R_i + R_O) * N_b$
C_b	stiffness constant, N/m$^{1\cdot5}$
C	damping constant, N s/m
K	stiffness, N/m
F_{θ_i}	spring force at the ball at angular location θi
F_x	x-component of the resultant spring force
F_y	y-component of the resultant spring force
F_u	unbalance force
T	time period
M	number of time samples for the HBM/AFT method
W	constant vertical force, N
$a_{X_{ij}}$, $a_{Y_{ij}}$, $b_{X_{ij}}$, $b_{Y_{ij}}$	coefficients of generalized Fourier series for X and Y displacements
$c_{X_{ij}}$, $c_{Y_{ij}}$, $d_{X_{ij}}$, $d_{Y_{ij}}$	coefficients of generalized Fourier series for forces F_x and F_y